

The PSF Smoothing Effect on Concentration-Related Parameters of High Redshift Galaxies in HST and JWST

Jia-Hui Wang^{1,2}, Zhao-Yu Li^{1,2*}, Ming-Yang Zhuang³, Luis C. Ho^{4,5}, and Li-Min Lai^{1,2}

¹ Department of Astronomy, School of Physics and Astronomy, Shanghai Jiao Tong University, 800 Dongchuan Road, Shanghai 200240, China

² Key Laboratory for Particle Astrophysics and Cosmology (MOE) / Shanghai Key Laboratory for Particle Physics and Cosmology, Shanghai 200240, China

³ Department of Astronomy, University of Illinois Urbana-Champaign, Urbana, IL 61801, USA

⁴ Kavli Institute for Astronomy and Astrophysics, Peking University, Beijing 100871, China

⁵ Department of Astronomy, School of Physics, Peking University, Beijing 100871, China

May 15, 2024

ABSTRACT

We perform a comprehensive investigation of the PSF smoothing effect on the measurement of concentration-related parameters (C , Gini, M_{20}) of high redshift galaxies in the HST and JWST surveys. Our sample contains massive galaxies ($10^{9.5}M_{\odot} \leq M_* \leq 10^{11.5}M_{\odot}$) from the CANDELS/EGS survey (at redshift $0 < z < 2$), and the CEERS survey (at redshift $1 < z < 3$). The non-parametric concentration-related parameters (R_{20} , R_{80} , C , Gini, M_{20}) and the model-dependent parameters (n , R_e) of these galaxies are derived from Statmorph and GALFIT, respectively. The best-fit Sérsic index (n) derived from image modelling is generally robust against the PSF smoothing effect and can be used to describe the intrinsic light distribution of galaxies. On the other hand, the concentration-related parameters are significantly affected by the PSF smoothing effect since they are directly calculated from the pixels of galaxy images. We try to evaluate the PSF smoothing effect by comparing the concentration-related parameters to the Sérsic index in both observations and mock images. We find that the concentration index is generally underestimated, especially for smaller galaxies with higher Sérsic index (eventually converging to the concentration index of the PSF). However, galaxies with lower Sérsic index ($n \leq 1$) or larger relative size ($R_e/\text{FWHM} > 3$) are less affected by the PSF smoothing effect. Tests with idealised mock images reveal that overestimating the measured R_{20}/R_e ratio leads to underestimating the concentration index C . Another commonly used concentration index C_{59} , derived from R_{50} and R_{90} values, is less affected by the PSF. The Gini coefficient and the absolute M_{20} statistic also show similar behaviour as the concentration index. Caution should be taken for the possible correction of the concentration-related parameters, where both the relative size and the Sérsic index of the galaxy are important. We also generate high redshift artificial images from the low redshift HST observations and confirm that the traditional correction method which simply adds a single term to the non-parametric indicators of galaxies at higher redshifts, is unable to reliably recover the true distribution of the structural parameters. Compared to the HST images, the PSF smoothing is much less severe for images in the CEERS survey (for the short-wavelength filters) due to the much higher spatial resolution. In fact, it is better to use the Sérsic index rather than the non-parametric morphology indicators to trace the light concentration for galaxies at high redshifts. From the single Sérsic modelling of the HST and JWST images, we also confirm that galaxies at higher redshift are more compact with smaller R_e . The lower mass galaxies are more disc-like ($n \sim 1$) compared to the higher mass galaxies that are more spheroid dominated ($n \sim 3$).

Key words. Galaxies: structure – Galaxies: fundamental parameters – Galaxies: evolution – Galaxies: high-redshift

1. Introduction

The morphology of a galaxy encodes important information about the physical processes that contributed to its formation and evolution (Conselice et al. 2008; Mortlock et al. 2013; Conselice et al. 2014; Huertas-Company et al. 2016). In Λ CDM cosmology, galaxies grow hierarchically (White & Rees 1978) and are shaped by both external and internal mechanisms such as mergers, tidal interactions, ram pressure stripping, starvation and harassment (Gunn & Gott 1972; Larson et al. 1980; Moore et al. 1996). On large time scales, galaxy evolution is dominated by secular processes i.e. a slow rearrangement of energy and mass involving the bar, spiral arms and dark matter halo (Kormendy & Kennicutt 2004).

Nearby galaxies are traditionally classified by their morphology according to the Hubble sequence (Hubble 1926), but it is

less straightforward to classify high redshift galaxies because of observational limitations or biases (Sandage 2005). In addition to the traditional visual classification, such as the Galaxy Zoo project (Lintott et al. 2011), more quantitative methods are also widely used, such as surface brightness profile analysis, single Sérsic component fitting, and multiple component fitting with bulge-disc decomposition (e.g. Sérsic 1968; Freeman 1970; Kormendy 1977b,a; Simien & de Vaucouleurs 1986; Caon et al. 1993; Peng et al. 2002; Simard et al. 2002; de Souza et al. 2004; Laurikainen et al. 2005; Gadotti 2008, 2009; Simard et al. 2011; Kormendy & Bender 2012; Bruce et al. 2014; Meert et al. 2015; Erwin 2015; Méndez-Abreu et al. 2017; Gao et al. 2018; Bottrell et al. 2019; Gao et al. 2020). These methods can be used to quantify the morphological parameters to trace the structural evolution of galaxies at both low and high redshifts (Trujillo et al. 2007; Buitrago et al. 2008; van der Wel et al. 2014; Allen et al. 2017; Whitney et al. 2019, 2020).

* Correspondence should be addressed to: lizy.astro@sjtu.edu.cn

Another widely used galaxy morphology classification is the non-parametric method in which morphological indicators are directly calculated from image pixels, without modelling the light distribution. Therefore, the advantage of using non-parametric methods for galaxy classification is that no a-priori assumptions about a galaxy model are needed. Some of the morphological indicators that can be derived in this way are the concentration index (C), the asymmetry index (A), the clumpiness index (S), the Gini coefficient (G) and the second-order moment of the brightest 20% of the galaxy light (M_{20}) (Kent 1985; Conselice et al. 2000; Conselice 2003; Lotz et al. 2004, 2008). These values enable an unbiased quantification of galaxy morphology, facilitating comparison with various physical properties (mass, size, colour, starformation rate, etc.) in order to gain a better understanding of the structural growth and evolution of galaxies. (Rodríguez-Gomez et al. 2019; Yesuf et al. 2021; Whitney et al. 2021; Nersesian et al. 2023; Yao et al. 2023). The non-parametric morphology indicators can also be used to separate galaxies into spheroids, discs and merging galaxies in the C - A and G - M_{20} spaces (Conselice 2003; Conselice et al. 2008; Lotz et al. 2008; López-Sanjuan et al. 2009). However, for high redshift galaxies, these measurements could be biased due to the smoothing effect of the point spread function (PSF) quantifying the light spread of a point source on the detector. The ‘spread’ is actually a blurring effect caused by various factors such as atmosphere turbulence (for ground observations), lens imperfections, mirror diffraction, detector limitations, observing filters etc. It is important to understand the bias introduced by such effect on non-parametric indicators before any scientific analysis can be performed.

Recently, Whitney et al. (2021) estimated the non-parametric morphology indicators in high redshift galaxies ($0.5 < z < 3$) in the Cosmic Assembly Near-IR Deep Extragalactic Legacy Survey (CANDELS) of the Hubble Space Telescope (HST) and confirmed that galaxies are more concentrated (have larger C values) at higher redshifts. In addition, Yao et al. (2023) analysed similar redshift galaxies ($0.8 < z < 3$) in the Cosmic Evolution Early Release Science (CEERS) survey of the James Webb Space Telescope (JWST) and found that the concentration index actually decreases for galaxies at higher redshift with $M_* > 10^{10}M_\odot$, in contrast with the findings of Whitney et al. (2021). In fact, the JWST telescope has revealed an unexpected high fraction of discs in the early Universe, at $z > 3$ (Kartaltepe et al. 2023; Sun et al. 2023; Ferreira et al. 2023), classified by either the Sérsic index or the non-parametric morphological indicators.

To properly account for the redshift effect on the morphology indicators, previous works have used $z \sim 1$ images to create mock galaxy images at high redshift (Whitney et al. 2021). The structural parameters of the mock images are then compared with the true values to derive an empirical correction for the non-parametric morphology indicators obtained from observations. Recently, Yu et al. (2023) improved the method by considering the ratio of the galaxy size (i.e. the Petrosian radius R_p ¹) to the PSF full-width-at-half-maximum (FWHM) as an additional parameter (R_p/FWHM). They used the nearby galaxy images from the Dark Energy Spectroscopic Instrument (DESI) to generate artificial images of high redshift galaxies observed in the CEERS survey, and found that the PSF smoothing leads to an underestimation of the concentration index (C) that is more severe for the galaxies of higher intrinsic C values. They also found that the dispersion of the corrected C value increases with decreasing

R_p/FWHM (see their Fig. 9). On the other hand, since the angular resolution of the JWST galaxies at $0.8 < z < 3$ is roughly similar, such empirical corrections were not considered in Yao et al. (2023). In the JWST era, to better understand the evolution of high redshift galaxies, it is important to evaluate the robustness of these non-parametric structural quantities and their corrections. In fact, Andrae et al. (2011) has already discussed the limits of the non-parametric structural measurements and concluded that they cannot be estimated independently from the images without potentially introducing serious biases. As shown in Davari et al. (2014), the Sérsic index and the effective radius of high redshift galaxies can be well recovered by 2D image modelling over a wide range of signal-to-noise ratios (S/N). Therefore, the Sérsic index can be used to reflect the intrinsic light profile shape of high redshift galaxies (Trujillo et al. 2001; Graham et al. 2005).

In this work, we mainly focus on the concentration-related quantities (C , Gini, M_{20}) since they are sensitive to the galaxy light distribution which suffers the most from the effect of PSF smoothing. The asymmetry (A) and clumpiness (S) indices are more affected by poor visibility of the outer region of galaxies due to surface brightness dimming. We decide to not include A and S in this study to avoid over-interpretation of our test results. To better evaluate the PSF smoothing effect on the concentration-related quantities, we compare the C , Gini, M_{20} values and the Sérsic index of high redshift galaxies from the Extended Groth Strip (EGS) field in CANDELS (Grogan et al. 2011; Koekemoer et al. 2011) and CEERS (Finkelstein et al. 2023). Mock images with different Sérsic indices are also constructed and analysed to help understand the reason for such bias.

The paper is organised as follows. The data and methods are described in Sect. 2 and 3, respectively. Sect. 4 presents the main results while Sect. 5 compares our results with previous works, and further investigates the effect of PSF smoothing for different light profile shapes using mock images. The results are summarised in Sect. 6.

2. Data

Our data sample consists of two sets of images: the first from the CANDELS/EGS survey (Grogan et al. 2011; Koekemoer et al. 2011), taken with the Advanced Camera for Surveys (ACS) and the Wide Field Camera 3 infrared channel (WFC3/IR) on HST; the second from the CEERS survey (Finkelstein et al. 2023), taken with the Near Infrared Camera (NIRCam) on JWST.

2.1. HST EGS

The EGS mosaic was produced following Koekemoer et al. (2011), with a pixel scale of $0.06''/\text{pixel}$. The ACS images have ~ 6000 s and $\sim 12,000$ s exposure times in the F606W and F814W filters respectively, reaching the 5σ depth of 28.8 and 28.2 mag (Stefanon et al. 2017). The WFC3/IR images have ~ 1300 s and ~ 2700 s exposure times in the F125W and F160W filters, both reaching the AB limiting magnitude of 27.6 mag. From the EGS catalogue (Stefanon et al. 2017), we choose a sample of galaxies at $0 < z < 2$ with stellar masses within $10^{9.5}M_\odot \leq M_* \leq 10^{11.5}M_\odot$, to ensure sample completeness. According to the morphological catalogue² in ?, only the spheroids and discs are selected in the following analysis. We exclude irregular galaxies to avoid large uncertainties in the measurements. For the photometric redshifts and stellar mass measurements, the median values of

¹ R_p is defined as the radius where the surface brightness is 20% of the average surface brightness within R_p (Petrosian 1976).

² http://rainbowx.fis.ucm.es/Rainbow_navigator_public/

Table 1. Properties of the sample

| z | Filter Name | λ_{rest} (Å) | FWHM (arcsec) | Number | Depth (mag) |
|------|-------------|--------------------------------|------------------|--------|----------------|
| (1) | (2) | (3) | (4) | (5) | (6) |
| 0.25 | F606W | 4850 | 0.122 | 175 | 28.8 |
| 0.75 | F814W | 4650 | 0.123 | 614 | 28.2 |
| 1.25 | F125W | 5550 | 0.194 | 850 | 27.6 |
| 1.75 | F160W | 5820 | 0.195 | 666 | 27.6 |
| 1.25 | F115W | 5110 | 0.049 | 149 | 29.2 |
| 1.75 | F150W | 5450 | 0.054 | 182 | 29.0 |
| 2.25 | F150W | 4610 | 0.054 | 113 | 29.0 |
| 2.75 | F200W | 5330 | 0.070 | 80 | 29.2 |

Notes. The top four rows with redshift range $0 < z < 2$ are from the EGS images. The bottom four rows with redshift range $1 < z < 3$ are from the CEERS images. Column 1 gives the midpoint of each redshift bin with $\Delta z = 0.5$. Column 2 gives the filter name. Column 3 gives the corresponding rest-frame wavelength. Column 4 gives the PSF FWHM for each filter. Column 5 gives the number of the galaxies. Column 6 gives the 5σ depths in the AB limiting magnitude.

the different estimations from Stefanon et al. (2017) are adopted. The images in different filters have different redshift ranges to ensure a similar rest-frame optical wavelength. The properties of the HST sample are shown in the top four rows of Table 1. We use GALAPAGOS (Barden et al. 2012) to generate cutouts of galaxies, encompassing twice the Kron ellipse (Kron 1980). The size of the cutout is sufficient for background measurement and photometric analysis. The segmentation map of nearby objects is convolved with the Tophat2DKernel(5) from Astropy (Astropy Collaboration et al. 2022) to smooth the edges of the segment; the mask image is then generated for the F160W mosaic cutout.

Galaxies observed at different wavelengths exhibit different structures causing the non-parametric morphology indicators to vary with wavelength (Baes et al. 2020; Nersesian et al. 2023; Yao et al. 2023). We measure all the structural quantities in the rest-frame wavelength at approximately $\lambda_{\text{rest}} \approx 4000 - 6000\text{Å}$, to avoid wavelength dependent variations. The rest-frame wavelengths of each filter are also listed in Table 1 for each redshift. The PSF FWHM and the number of the galaxies for each filter are also listed. The PSF is empirically constructed using the bright and non-saturated field stars (see Sect. 3.3). To ensure robust structural measurements, we limit our EGS sample to galaxies above a minimum S/N of 3 and $R_p > 5$ pixels and obtain 2305 galaxies. More details about the influence of the S/N on the morphology indicators are shown in Sect. 3.4.

2.2. JWST CEERS

The NIRCcam imaging of CEERS covers a total of 100arcmin^2 in the F115W, F150W, F200W, F277W, F356W, F410M, and F444W filters down to a 5σ depth ranging from 28.8 to 29.7 mag (Finkelstein et al. 2023). The first set of CEERS observations was taken on 21 June 2022 in four pointings in the EGS field. The image mosaic with a pixel scale of $0.03''/\text{pixel}$ has additional corrections such as snowballs, wisps, $1/f$ noise, and background subtraction. A detailed description of the reduction process can be found in Bagley et al. (2023). We choose galaxies with $1 < z < 3$ in the F115W, F150W, and F200W filters, which correspond to similar rest-frame optical wavelength. Finally, our JWST/CEERS sample contains 524 galaxies with

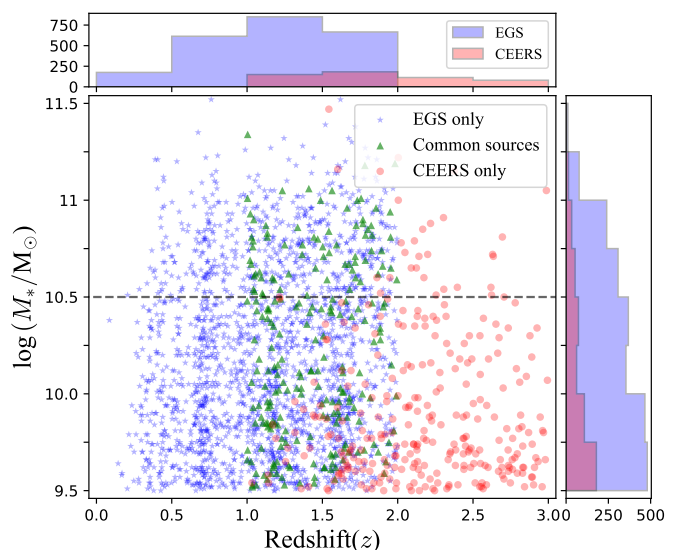


Fig. 1. Mass and redshift distribution of the galaxies in our sample. The blue stars indicate galaxies in the EGS images, and the red circles indicate galaxies in the CEERS images. The green triangles indicate the common sources between the EGS and CEERS images. The dashed horizontal line at $\log(M_*/M_\odot) = 10.5$ indicates the boundary between the high-mass galaxies and low-mass galaxies in this study.

$S/N > 3$ and $R_p > 5$ pixels (Stefanon et al. 2017). The properties of the CEERS images are given in the bottom four rows of Table 1.

Fig. 1 shows the mass and redshift distribution of our sample. The blue stars indicate the galaxies in the EGS images, and the red circles indicate the galaxies in the CEERS images. There are 228 galaxies (green triangles) in common between the EGS and CEERS images. In Sect. 5.4, the structural parameters of the common sources are compared for consistency checks.

3. Methods

This section describes the method employed to measure the structural parameters (C , Gini, M_{20} , Sérsic index n and effective radius R_e), the PSF construction and the S/N test.

3.1. Structural quantities measurement

The concentration index quantifies how much light is distributed in the centre of a galaxy as opposed to its outer parts (Conselice 2003),

$$C = 5 \log \left(\frac{R_{80}}{R_{20}} \right), \quad (1)$$

where R_{20} and R_{80} are the radii of circular apertures containing 20 and 80 percent of the Petrosian flux, respectively. The Petrosian flux is defined as the flux within $1.5R_p$.

The Gini coefficient is traditionally used in economics to quantify the wealth inequality in a population; in astronomy, it is used to quantify the relative distribution of the flux within a galaxy. It is related to the light concentration but differs from the concentration index; the Gini coefficient only accounts for the clustering of bright pixels, regardless of their spatial distributions e.g. whether these bright pixels are distributed in the galaxy centre or outskirts (Abraham et al. 2003; Lotz et al. 2004). Assuming that a galaxy image has n pixels with flux I_i in each pixel, the Gini coefficient can be computed as (Glasser 1962),

$$G = \frac{1}{|\bar{I}|n(n-1)} \sum_{i=1}^n (2i-n-1)|I_i|, \quad (2)$$

where $|I_i|$ indicates the i -th brightest pixel, and $|\bar{I}|$ represents the mean value of the pixels. $G = 1$ is obtained when all of the flux is concentrated in a single pixel, while a homogeneous brightness distribution yields $G = 0$. The Gini coefficient depends on the S/N (Lisker 2008), which is tested in Sect. 3.4.

The second-order moment statistic is similar to the concentration index in that it indicates whether the light is concentrated within an image (not necessarily in the centre but at any location in the galaxy) (Lotz et al. 2004). The total second-order central moment, M_{tot} , is calculated as

$$M_{\text{tot}} = \sum_{i=1}^n M_i \equiv \sum_{i=1}^n I_i [(x_i - x_c)^2 + (y_i - y_c)^2], \quad (3)$$

where (x_i, y_i) , (x_c, y_c) are the positions of a pixel and the galaxy centre, respectively. I_i is i -th brightest pixel value. M_{20} is defined as the normalised second-order moment of the brightest 20% of the total flux,

$$M_{20} \equiv \log \left(\frac{\sum_i M_i}{M_{\text{tot}}} \right), \text{ while } \sum_i I_i < 0.2I_{\text{tot}}. \quad (4)$$

In particular, Lotz et al. (2008) suggested that the G - M_{20} space can be used to roughly separate spheroids, discs, and merging galaxies at $0.2 < z < 0.4$. The PSF smoothing effect on the distribution of galaxies in the G - M_{20} space will also be examined in Sect. 4.2.

n and R_e are derived by fitting the galaxy image with GALFIT (Peng et al. 2002, 2010) using a single Sérsic component (Sérsic 1968). The fitting parameters include galaxy centre, total magnitude (m), R_e measured along the major axis, n , axis ratio (q), and position angle (P.A.). Initial guesses for these parameters are taken from the Statmorph output. We fix the sky value as the median of pixels in four background regions around the galaxy (usually ~ 0). Our fitting results are generally consistent with van der Wel et al. (2012).

3.2. Correlation between the concentration index and the Sérsic index

Both the Sérsic index and the concentration index reflect the shape of the light profile. Utilising the fact that R_{20} and R_{80} contain 20% and 80% of the total flux respectively, the relationship between C and n for a given Sérsic profile can be derived numerically. As shown in Andrae et al. (2011), the relationship can be approximated as

$$C \approx 2.586 n^{0.305}. \quad (5)$$

Andrae et al. (2011) has used galaxies in the COSMOS survey to demonstrate that C and n are statistically consistent, but exhibiting a large scatter. Similar to Andrae et al. (2011), we also plot the distribution of EGS images in the C - n space in Fig. 2. We can see that the galaxies with the large relative sizes ($R_e/\text{FWHM} > 3$, blue) generally follow the expected numerical relationship. Therefore, the Sérsic index can be an estimate of the intrinsic concentration of a galaxy (Trujillo et al. 2001; Graham et al. 2005). However, those with the smaller sizes ($R_e/\text{FWHM} \leq 1$, dark red) have significantly underestimated concentration index.

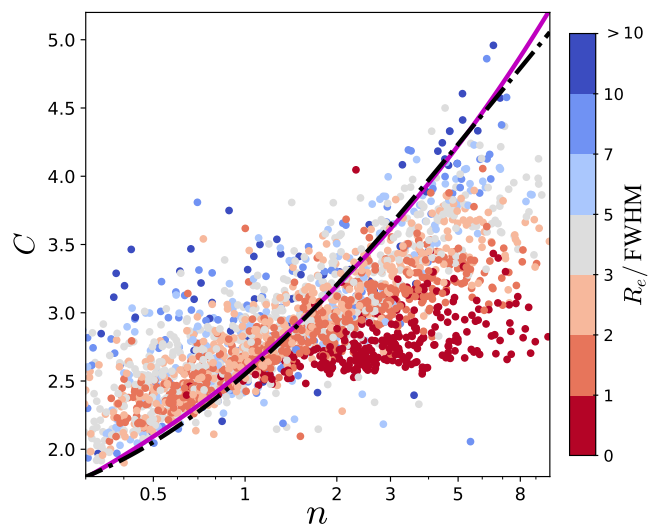


Fig. 2. Correlation between the concentration index and the Sérsic index for the EGS images. The black dot-dashed curve is the numerical relationship derived by integrating the best-fit Sérsic model out to $1.5R_p$. The purple solid curve is the empirical relationship of Eq. (5). The colour of the points marks the relative size of the galaxies (R_e/FWHM). The data points generally agree with the numerical expectation, but showing large scatters, especially for the galaxies with the smaller relative sizes ($R_e/\text{FWHM} \leq 1$).

In fact, the directly measured C values (without correction) of high redshift galaxies, are usually smaller than the C values of lower redshift galaxies. R_{20} and R_{80} are the two key parameters in the derivation of the C value (see Eq. 1): since R_{20} is closer to the central region of the galaxy, it is more overestimated than R_{80} , resulting in a lower C value. Since the Sérsic index is derived from image modelling including PSF smoothing, it is a more reliable indicator of the light profile shapes of high redshift galaxies (Trujillo et al. 2007; Davari et al. 2014).

3.3. PSF construction

In the photometric analysis of the HST and JWST images, it is customary to build the PSF models using point sources in the image. Following Zhuang & Shen (2023), we use SExtractor (Bertin & Arnouts 1996) to perform source detection to select point sources of high signal-to-noise ratio, non-blended, non-irregular, unsaturated, and without any bad pixels. We then use PSFEx (Bertin 2011) to construct the PSF models. We generate PSF models with the cutout size of 121×121 pixels ($\sim 7.2'' \times 7.2''$) for the EGS filters and 131×131 pixels ($\sim 3.9'' \times 3.9''$) for the CEERS filters; the PSF images are sufficiently large, encompassing at least twice the radius that encloses 98% of the total flux ($\sim 1.7''$ for EGS and $\sim 0.95''$ for CEERS). The PSFs of the EGS and CEERS images have the pixel scales of $0.06''/\text{pixel}$ and $0.03''/\text{pixel}$, respectively. The FWHMs of all the PSF models are listed in Table 1. In Fig. 3, we show the normalised surface brightness profiles and the growth curves of the PSF models for the EGS and CEERS mosaics in the top and bottom panels, respectively.

3.4. S/N test

In order to evaluate the influence of S/N on the morphological indicators, we simulate 5000 mock galaxies with 200×200 pixels, where the pixel scale is $0.06''/\text{pixel}$. Each model is built

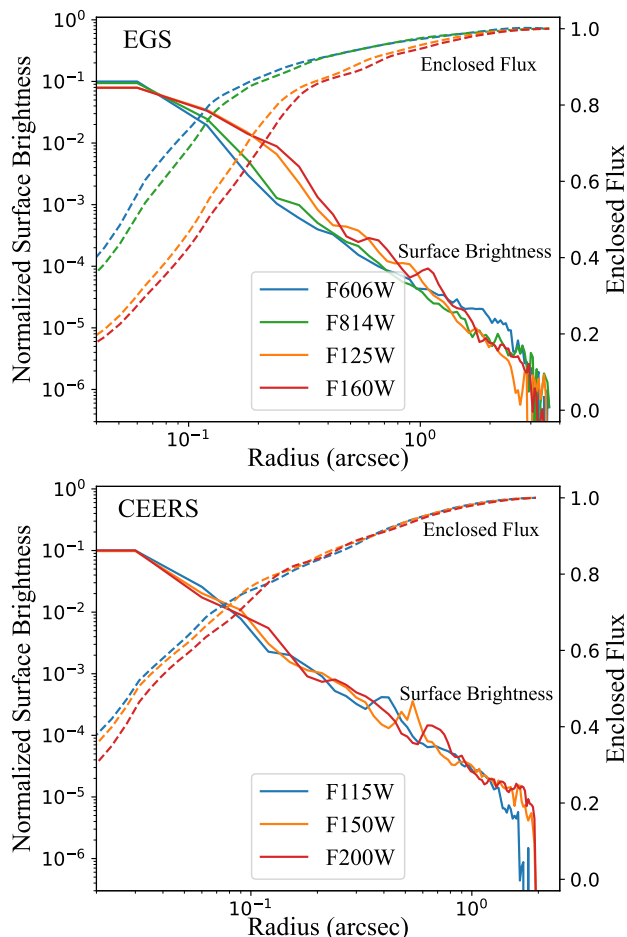


Fig. 3. The normalised surface brightness profiles (solid line) and the growth curves (dashed line) of the PSF models for EGS (top) and CEERS (bottom), colour-coded with different filters. The growth curves are normalised to the total flux of the PSF model within $7.2''$ (EGS) and $3.9''$ (CEERS).

by GALFIT using a single Sérsic component. The structural parameters are chosen randomly in the following ranges: $1.67 \leq R_e \leq 35$ pixels ($\sim 0.1'' - 2.1''$ in WFC3/F160W), $0.5 \leq n \leq 8$, and $0.2 \leq q \leq 0.9$. The magnitude range is $20 \leq m_H \leq 25$, corresponding to $1 \leq S/N \leq 20$. We first use Statmorph to calculate the intrinsic non-parametric morphological indicators of these idealised models. Then these images are multiplied by the exposure time of 2700s, and convolved with the PSF of the F160W band. We use `apply_poisson_noise` from Photutils (Bradley et al. 2022) to add Poisson noise with Gain = 2.5, and a real sky background from the EGS mosaics. After generating the mock galaxies, we use GALFIT to perform the single Sérsic component fit and Statmorph to calculate the non-parametric morphology indicators to examine the deviations.

The average S/N for each galaxy image is defined as

$$S/N = \frac{F_{\text{tot}}}{\sqrt{F_{\text{tot}} + q\pi R_p^2 \sigma_{\text{sky}}^2}}, \quad (6)$$

where F_{tot} is the total integrated flux within the Petrosian radius, and σ_{sky} is the standard deviation of the sky background. Fig. 4 shows the difference between the measured structural parameters and the intrinsic values as a function of S/N. We can see that the deviations increase with decreasing S/N. At lower S/N, the Sérsic index and R_e are slightly overestimated. The concentration-

related parameters (C , G , M_{20}) on the other hand, are all underestimated. In addition to the PSF smoothing effect, the outskirts of the galaxies at low S/N are also affected by the noise which reduces the total flux of the galaxy, resulting in smaller R_{80} , further decreasing the measured C value. For our working sample, we choose $S/N > 3$ to reduce uncertainties in the morphology indicators and the Sérsic index.

4. Results

In this section, we study the correlation between the concentration-related parameters and the Sérsic index in detail in order to understand the PSF smoothing effect. A subset of EGS and CEERS images are shown in Figs. 5 and 6, respectively, with the Sérsic index increasing from top to bottom (disc to spheroid morphology) and the redshift increasing from left to right.

The best-fit Sérsic index and the measured concentration-related parameters are also labelled in each panel. As shown in Fig. 5, the concentration indices are similar (~ 2.4) for discs with Sérsic index $n \sim 1$ at $z \approx 0$ to 2. However, the spheroids ($n > 4$) with smaller sizes tend to have lower C values. As the redshift increases, the concentration index drops from ~ 4.3 to ~ 3.4 for galaxies with Sérsic index $n \sim 5$. The PSF smoothing effect is more severe in this case. For the CEERS images shown in Fig. 6, the similar trend can still be observed, although it is not as significant as in the EGS images. This difference is attributed to the much higher spatial resolution provided by JWST.

4.1. PSF smoothing effect on the concentration index

4.1.1. The correlation between C and n

The measured R_{20}/R_e , R_{80}/R_e and C as a function of n with the EGS images at different redshifts are shown in Fig. 7. Note that R_{80}/R_e can be less than 1 for the galaxies with steep light profiles ($n \geq 5$). This is because R_{20} and R_{80} are measured out to $1.5R_p$ which may not be large enough to enclose the total flux of the galaxy (Graham et al. 2005). Additionally, due to the default circular aperture used in Statmorph, the R_{20} and R_{80} of galaxies with small axis ratio (close to edge-on) tend to be underestimated. This effect is further explored in Sect. 5.1; when we adopt the elliptical apertures with the same axis ratio as the galaxy outskirts, the underestimation is significantly reduced, especially for galaxies with low Sérsic index.

The numerical relations between the structural parameters (R_{20}/R_e , R_{80}/R_e , C) and the Sérsic index are over-plotted with a dot-dashed line³. The empirical relation of Eq. (5) is also plotted as the purple solid line. The agreement between the two curves is remarkable. The colour of each point indicates the R_e/FWHM ratio, representing the relative size of the galaxy compared to the PSF (red for smaller galaxies and blue for bigger ones).

At lower redshifts ($z \leq 1$), galaxies with $R_e/\text{FWHM} \geq 5$ (blue points) generally follow the theoretical relation between R_{20}/R_e (R_{80}/R_e) and n . As the redshift increases, the galaxies become smaller with much lower R_e/FWHM , with R_{20}/R_e overestimated up to a factor of 5 for smaller galaxies (i.e., the red points). R_{80}/R_e is also overestimated but not as significantly as R_{20}/R_e . Such deviation is less severe for galaxies with smaller Sérsic indices, even at higher redshifts.

Galaxies at lower redshifts with $R_e/\text{FWHM} > 3$ exhibit a strong correlation between C and n , consistent with the theoretic-

³ The numerical relation is derived by integrating the Sérsic model out to $1.5R_p$.

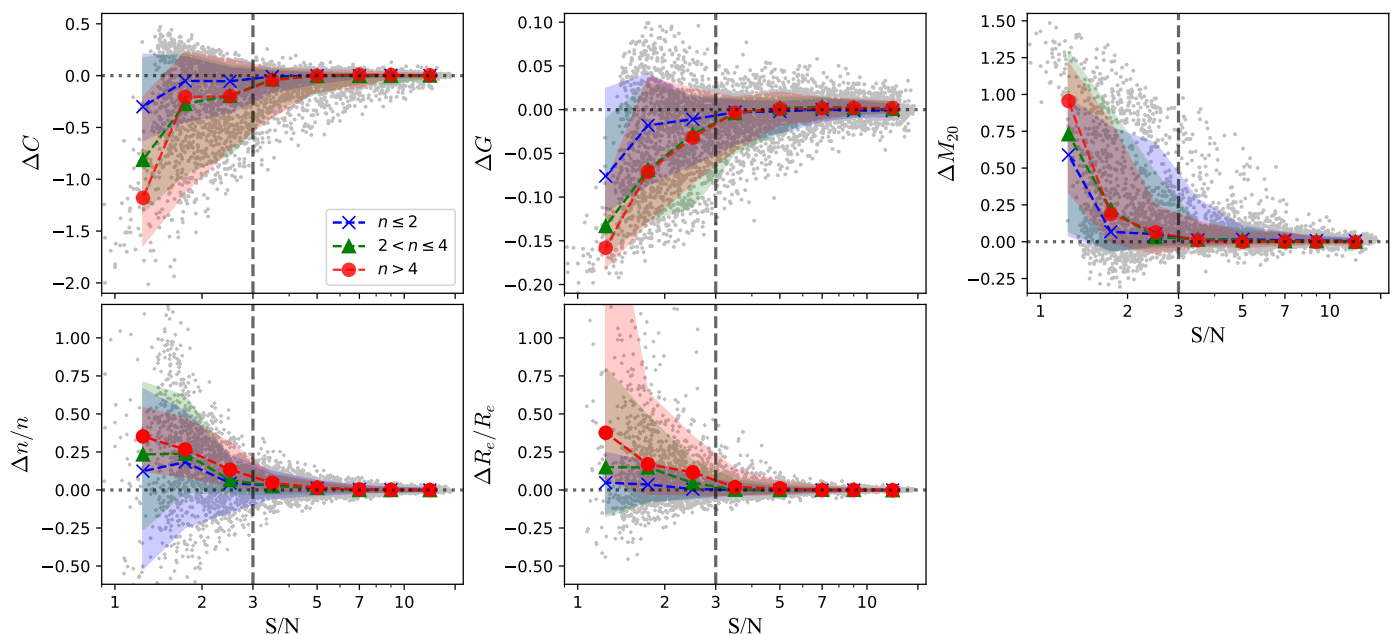


Fig. 4. Dependence of the morphology indicators uncertainties on S/N, estimated from mock images. The median trends of the mock galaxies with different n are marked with dotted lines; the shaded region indicates the 16th to 84th percentiles. The top row shows the difference between the measured parameters and the intrinsic values, expressed as $\Delta C = C_{\text{mock}} - C_{\text{int}}$. The bottom row shows the difference between the measured and true n and R_e values, relative to the true value. The horizontal dotted line at zero indicates perfect agreement between measurements and true values while the vertical dashed line marks the $S/N=3$ boundary beyond which the agreement considerably improves.

cal expectation. In addition, C and n of the higher redshift galaxies with $n < 2$ also have a good relationship, consistent with the theoretical curve. Only at higher Sérsic indices, the measured C values start to deviate from the theoretical expectation. It is noticeable that R_{20}/R_e is more significantly overestimated by the PSF smoothing effect than R_{80}/R_e for the smaller galaxies. According to Eq. (1), the concentration index is underestimated. As the galaxy becomes even smaller with $R_e/\text{FWHM} < 1$, the galaxy light profile is overshadowed by the PSF. The C values of the galaxies with different Sérsic indices all converge to roughly the same value (~ 2.7), corresponding to the PSF.

Our results confirm that the relative size and the Sérsic index are important parameters in the determination of the concentration index. Previous literature usually applied a correction factor to the directly measured C values of high redshift galaxies to account for such effect. However, for the CEERS images, the relationship between C and n still holds up to redshift $z \sim 3$, as shown in Fig. 8. This is mainly caused by the smaller PSF in JWST, with very few galaxies with $R_e/\text{FWHM} < 2$ in our sample. For JWST, therefore, a correction of the concentration index may not even be needed for high redshift galaxies ($1 < z < 3$).

4.1.2. The correlation between C_{59} and n

Another concentration index commonly used in literature is $C_{59} = 5 \log(R_{90}/R_{50})$, with R_{90} representing the radius enclosing 90% of the Petrosian flux (Blanton et al. 2001). It can also be used to distinguish discs from spheroids (Strateva et al. 2001; Kauffmann et al. 2003). The correlation between C_{59} and n for the EGS images at different redshifts is shown in Fig. 9. Similar to R_{20} and R_{80} , R_{50} and R_{90} are overestimated for small galaxies. However, R_{50} and R_{90} exhibit comparable levels of overestimation, resulting in the C_{59} values less affected by the PSF smoothing effect compared to the C values discussed before. Objects with $R_e/\text{FWHM} < 1$ are generally underestimated. We notice

that C_{59} for galaxies with lower n are overestimated, mainly due to single Sérsic component fitting might not adequately describe these galaxies. Moreover, C_{59} is less affected by the aperture axis ratio.

The empirical boundary between spheroids and discs is indicated by the horizontal dashed line at $C_{59} = 2$ (corresponding to $n \sim 3$) in the bottom rows of Fig. 9. Strateva et al. (2001) suggested $r_{90}/r_{50} = 2.6$ ($C_{59} \sim 2.07$ according to Eq. (1)) as the criterion, with $r_{90}/r_{50} > 2.6$ for spheroids, and $r_{90}/r_{50} < 2.6$ for discs. Here r_{90} and r_{50} are the radii of 90% and 50% flux within $2R_p$ (instead of $1.5R_p$ used in this work). It seems that this criteria works for galaxies with $R_e/\text{FWHM} \geq 2$.

As shown in Fig. 10, the R_{50} and R_{90} for the CEERS images are consistent with the numerical relationships, except for the smaller objects that are also slight overestimated. In this case, it seems that C_{59} is robust for galaxies with $R_e/\text{FWHM} > 1$ with no correction needed.

4.2. PSF smoothing effect on the Gini and M_{20} statistics

The relationship between G and M_{20} with respect to n for the EGS images is shown in the top two rows of Fig. 11. The galaxies at higher redshifts roughly follow the dashed line of the low redshift sample, as indicated by the black dashed line for $z < 1^4$, but with substantial scatters, especially for the galaxies with lower R_e/FWHM . At $z \geq 1$, the G values of the high Sérsic index galaxies with $R_e/\text{FWHM} \leq 2$ are generally lower than the low redshift relation (i.e., the dashed line). Generally speaking, due to the PSF smoothing effect, the Gini coefficient is underes-

⁴ In practice, a numerical relationship between G (M_{20}) and n cannot be directly obtained. The two indicators are derived from the pixel values of the galaxy image, which depend on the structure of the galaxy. M_{20} is also sensitive to the off-centre bright clumps in the discs. Note that we have selected galaxies with $R_e/\text{FWHM} > 5$ in this redshift range to ensure less PSF smoothing effect in these two parameters.

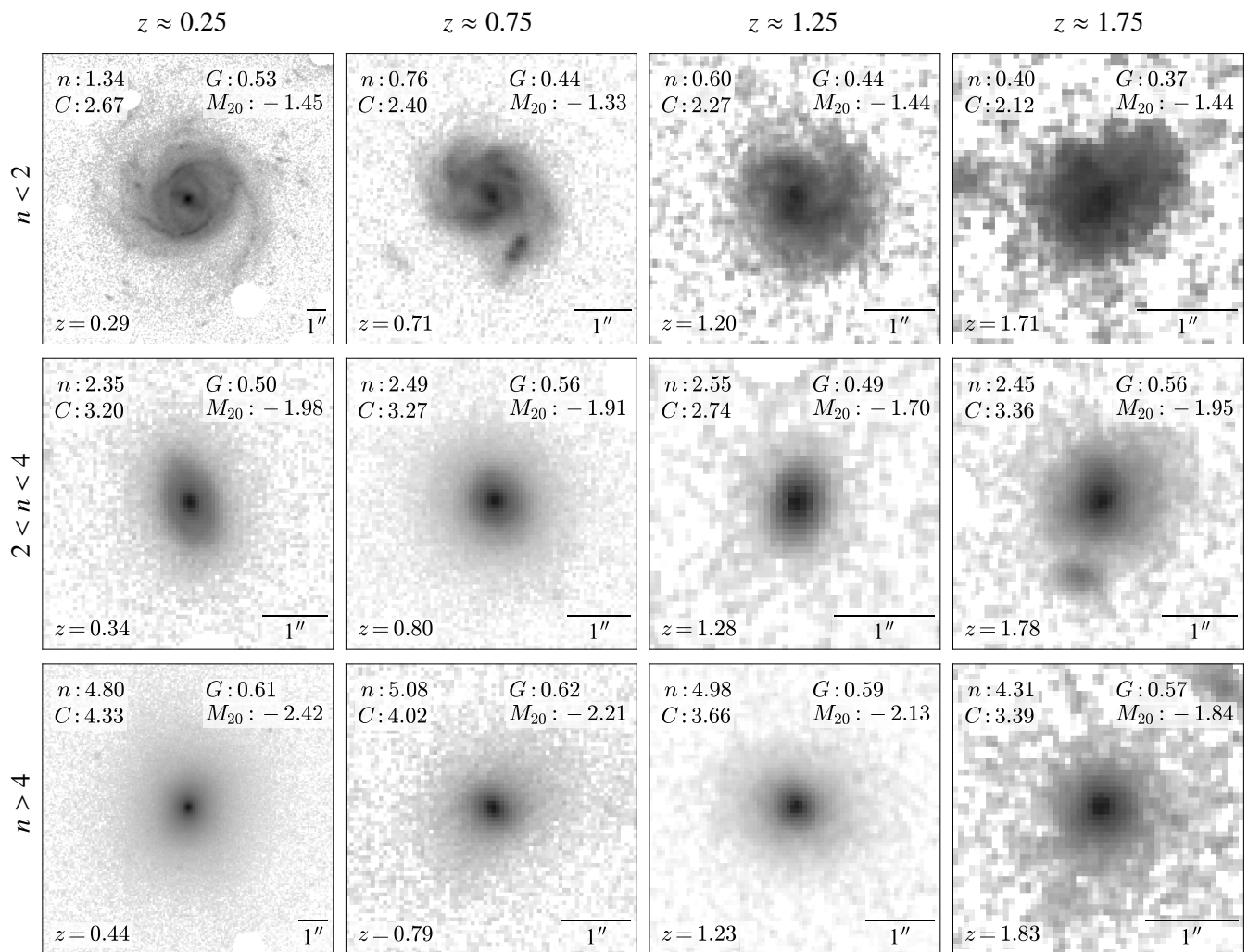


Fig. 5. Examples of galaxies in the EGS images, with the Sérsic index increasing from the top to bottom rows (disc to spheroid morphology) and the redshift increasing (from $z \approx 0$ to 2) from the left to right columns. The filters have been selected to have the similar rest-frame optical wavelength. The measured structural parameters (n , C , G , M_{20}) are also listed in each panel. The galaxies on the right two columns are also observed in CEERS, which are shown in the left two columns of Fig. 6

timated, but not as significant as the concentration index shown in Fig. 7.

At $z = 0.25 - 0.75$, M_{20} exhibits a strong correlation with the Sérsic index, whereas the correlation becomes flattened at higher redshifts. Note that for galaxies with $n \leq 2$, M_{20} is slightly lower (with higher absolute values) than the low redshift relationship as shown in the left panel. As the galaxy image loses the fine structures at higher redshifts due to the surface brightness dimming and poor spatial resolution, the bright clumps distributed across the galaxy have been washed out to result in lower M_{20} . Good examples are shown in right two columns of Fig. 5 and left two columns of Fig. 6, as the discs observed by HST look much more smooth than those observed by JWST. At higher Sérsic indices, as the PSF smoothing effect is more significant, M_{20} is systematically higher (with lower absolute values) than the low redshift one.

The distribution of the galaxies at different redshifts in the G - M_{20} space is shown in the bottom panel of Fig. 11. The black dashed lines are the boundaries between different galaxy types from Lotz et al. (2008), for $0.2 < z < 1.2$ EGS galaxies as fol-

lowing:

$$\begin{aligned}
 \text{Merger} & : G > -0.14M_{20} + 0.33, \\
 \text{E - Sa} & : G \leq -0.14M_{20} + 0.33, G > 0.14M_{20} + 0.80, \\
 \text{Sb - Irr} & : G \leq -0.14M_{20} + 0.33, G \leq 0.14M_{20} + 0.80.
 \end{aligned} \tag{7}$$

Focusing on the E-Sa and Sb-Irr regions, at $z \sim 0.5$, the dashed line provides a clear demarcation between the two regions. Most points with $n \leq 3$ are located in the Sb-Irr region. With the redshift increasing, the Sb-Irr region is gradually populated by galaxies with high Sérsic indices. For all $n > 4$ galaxies, at $z = 0.25$, no object resides in the Sb-Irr region. And the fraction of the $n > 4$ galaxies in this region becomes 5% for $z = 0.75$ (5 in 99), 26% for $z = 1.25$ (20 in 77), and 52% for $z = 1.75$ (37 in 71). It seems that the empirical classifications of the galaxy morphology works well at lower redshifts. At higher redshifts, due to the observational bias, a significant fraction of the galaxies with high Sérsic indices would be misclassified as discs in the G - M_{20} space. Lotz et al. (2008) has shown that, as the redshift increases, the observed Sb-Irr fraction rises, while the observed fraction of E-Sa declines. Consistent with our result, this trend suggests that the distribution of the galaxies in G - M_{20} space is

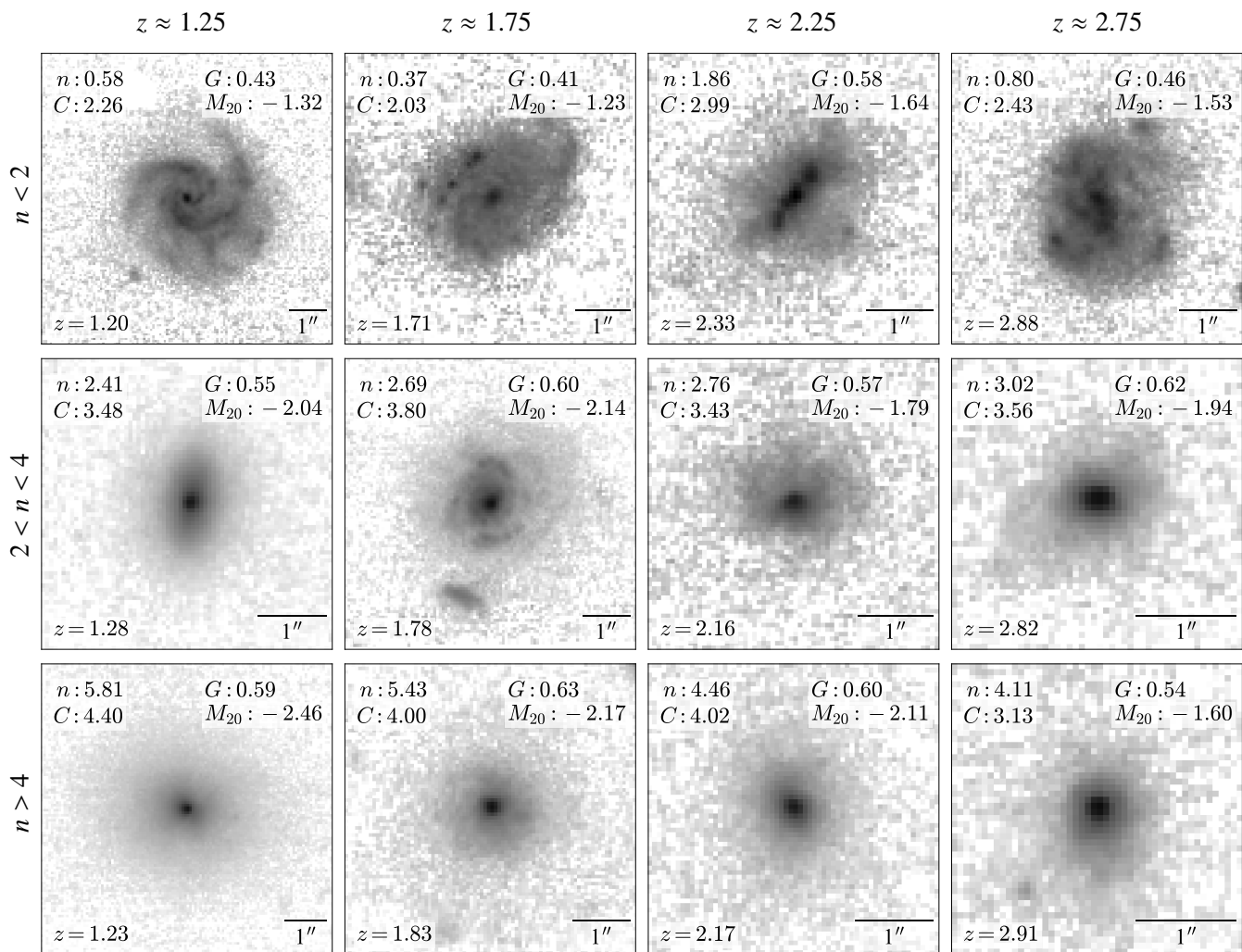


Fig. 6. Examples of galaxies in the CEERS images, with the Sérsic index increasing from the top to bottom rows (disc to spheroid morphology) and the redshift increasing (from $z \approx 1$ to 3) from the left to right columns. The structural parameters are also listed in each panel. The galaxies on the left two columns are also shown in the same as ones in the right two columns of Fig. 5 for the HST observation. Due to the higher resolution and S/N of images in JWST, the galaxies exhibit more details, resulting in higher values of C , G , and $|M_{20}|$ for galaxies with $n > 2$.

affected by the PSF smoothing effect, leading to inaccurate interpolations of their morphologies. In this case, simply correcting the G or M_{20} values (e.g. a systematic shift for all the G and M_{20} values measured at the high redshift) would not help to improve the separation of the galaxies with different morphologies, since these galaxies are mixed together in the G - M_{20} space.

For the CEERS images, both G and M_{20} are less affected by the PSF smoothing effect at each redshift bin ($1 < z < 3$), as shown in Fig. 12. This is attributed to the higher spatial resolution in JWST. The empirical separation between the $n > 2.5$ and $n < 2.5$ galaxies in the G - M_{20} space also works well at different redshifts.

5. Discussion

As we have shown, the PSF smoothing effect could significantly affect the measured non-parametric morphology indicators, especially for the galaxies with smaller sizes and higher Sérsic indices. The traditional correction strategy by adding a single term to all the galaxies in a given high redshift range could not properly account for such a complexity. In this section, the observational bias and problems with the previous correction methods are investigated and discussed in detail.

5.1. Effect of the galaxy axis ratio

In the galaxy size measurement, the R_{20} and R_{80} values are determined using a circular annulus via the curve of growth method (out to $1.5R_p$) in Statmorph, while R_e is derived from the single Sérsic component fit using GALFIT. Andrae et al. (2011) suggested that the concentration index can be influenced by the aperture axis ratio. For $q < 0.5$, the concentration index measured with the circular aperture could be substantially overestimated (even up to 30% for galaxies with $n = 1$).

It is noticeable that in the C - n space, the distribution of galaxies with $n \leq 2$ scatter around the expected correlation in Fig. 7. Most of these objects are close to edge-on, with examples shown in the left three panels of Fig. 13. Here C' is the concentration index measured in the elliptical apertures with the same axis ratio as the galaxy outskirts. Galaxies in the left three panels with small axis ratios ($q < 0.3$) have $C > C'$, while the face-on galaxy in the right panel has similar C' and C . Note that the four galaxies have the similar Sérsic index ($n \sim 1$), implying that their intrinsic C values should also be similar. Indeed, after adopting the ellipse aperture, the C' values of these galaxies are all ~ 2.5 . It is necessary to use elliptical isophotes to get an ac-

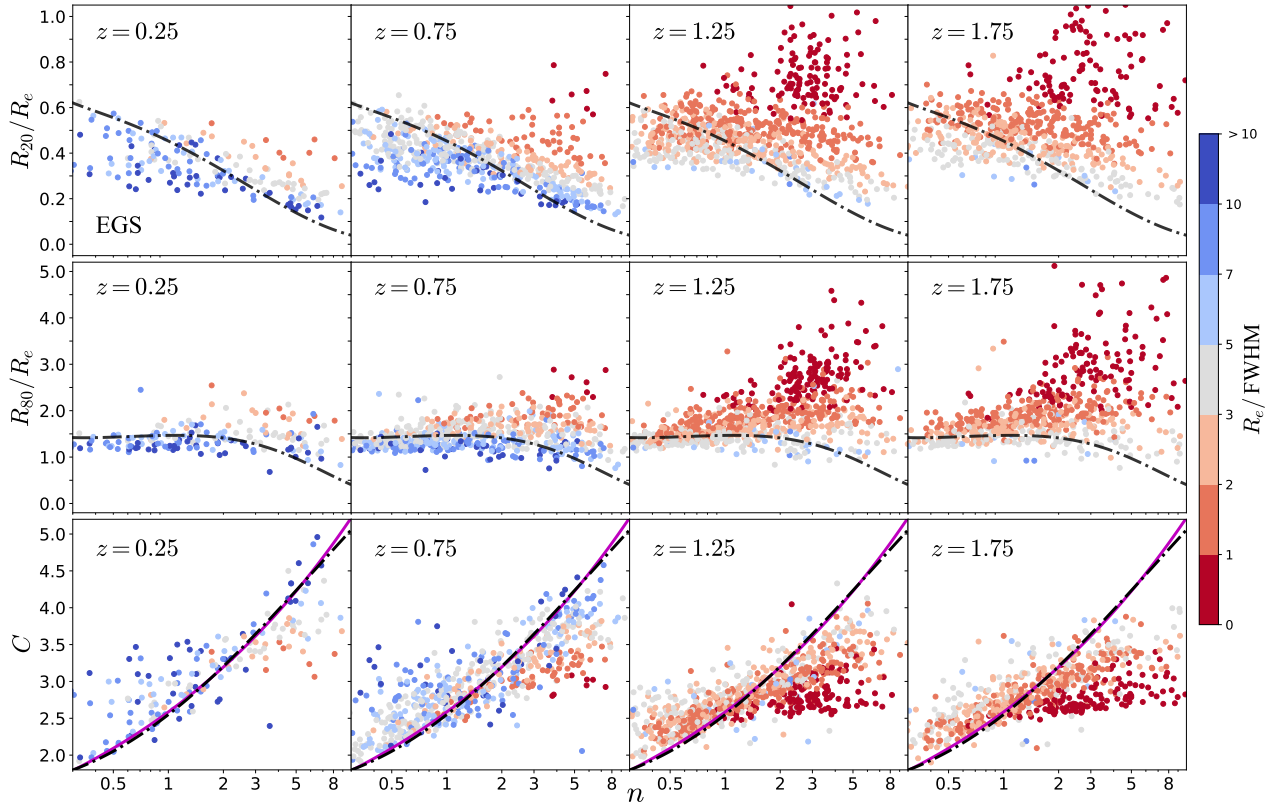


Fig. 7. R_{20}/R_e , R_{80}/R_e and C as the Sérsic index a function of n for the EGS images at $0 < z < 2$. The black dot-dashed curve in each panel is the numerical correlations derived by integrating the Sérsic profile. In the bottom row, the purple solid curve is the empirical relation of Eq. (5) given by Andrae et al. (2011). The colour of the points marks the relative sizes of the galaxies with R_e/FWHM .

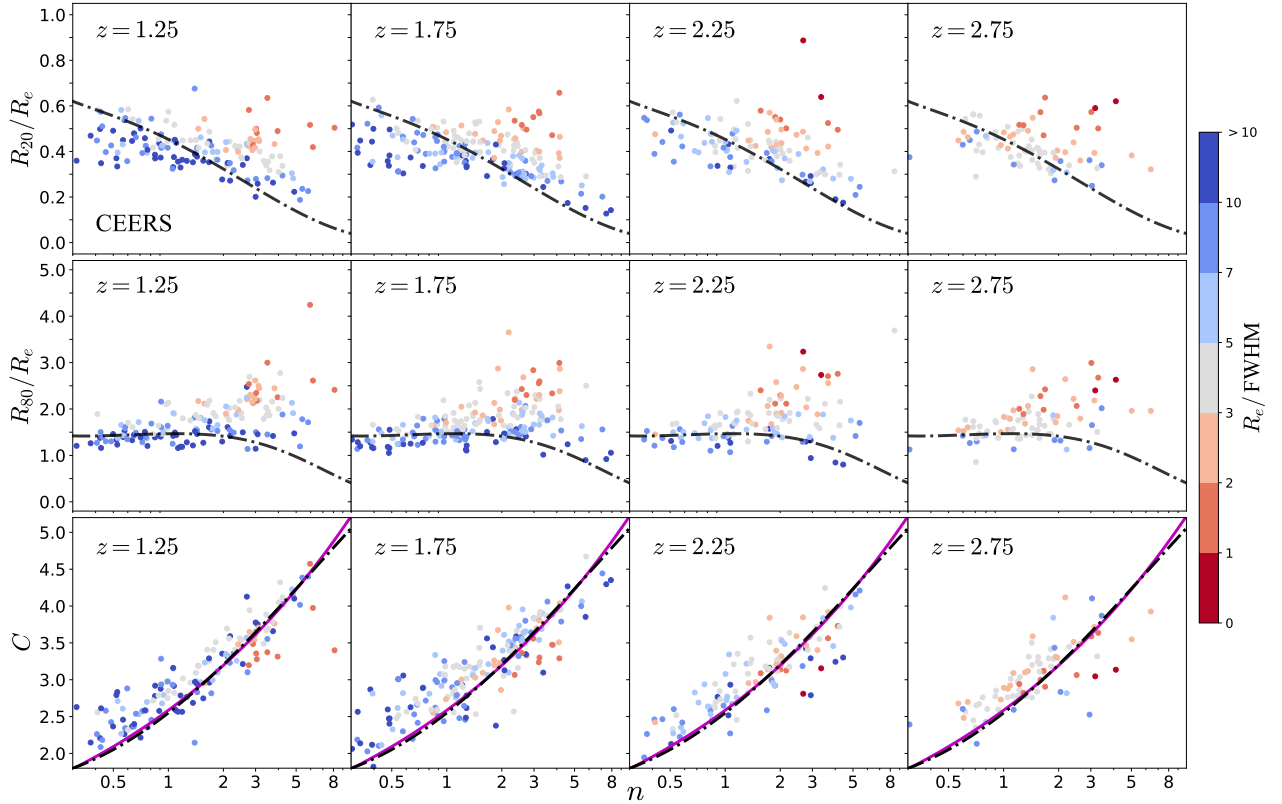


Fig. 8. Same as Fig. 7, but for the CEERS images at $1 < z < 3$. There is very few galaxies with extremely small size ($R_e/\text{FWHM} \leq 1$). The overall agreement between C and n are quite good consistent with the numerical relationship different redshifts.

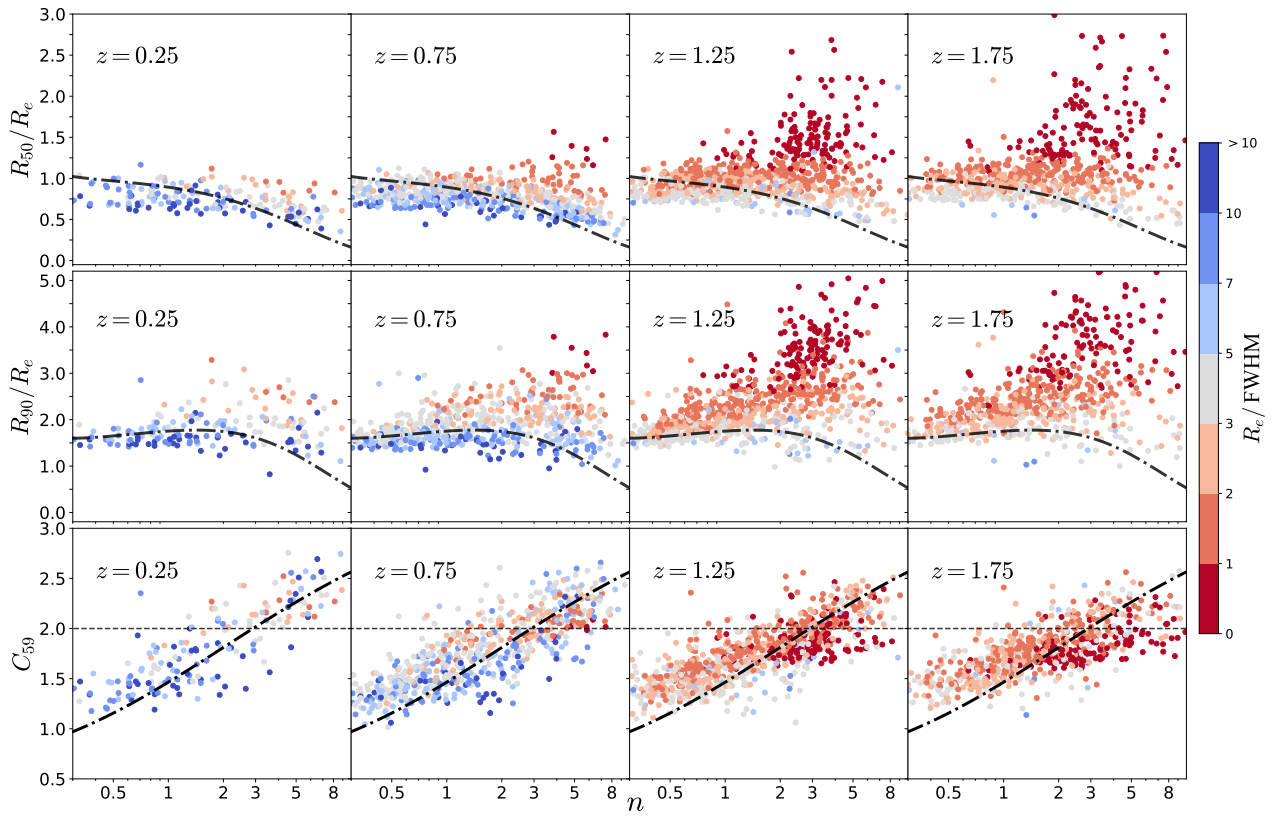


Fig. 9. R_{50}/R_e , R_{90}/R_e and C_{59} as a function of the Sérsic index n for the EGS images at $0 < z < 2$. The black dot-dashed curve in each panel is the numerical correlations derived by integrating the Sérsic profile. In the bottom row, the horizontal dashed line $C_{59} = 2$ indicates the empirical boundary between spheroids and discs.

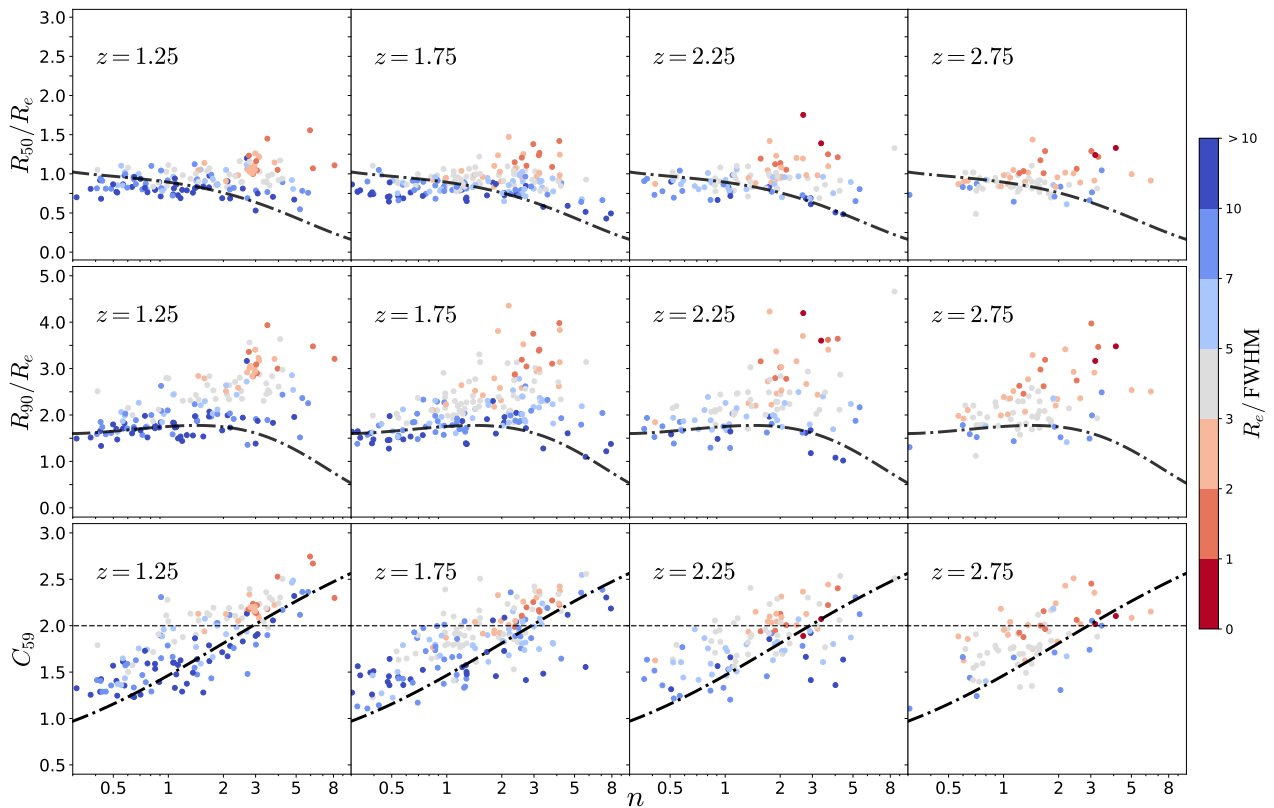


Fig. 10. Same as Fig. 9, but for the CEERS images at $1 < z < 3$.

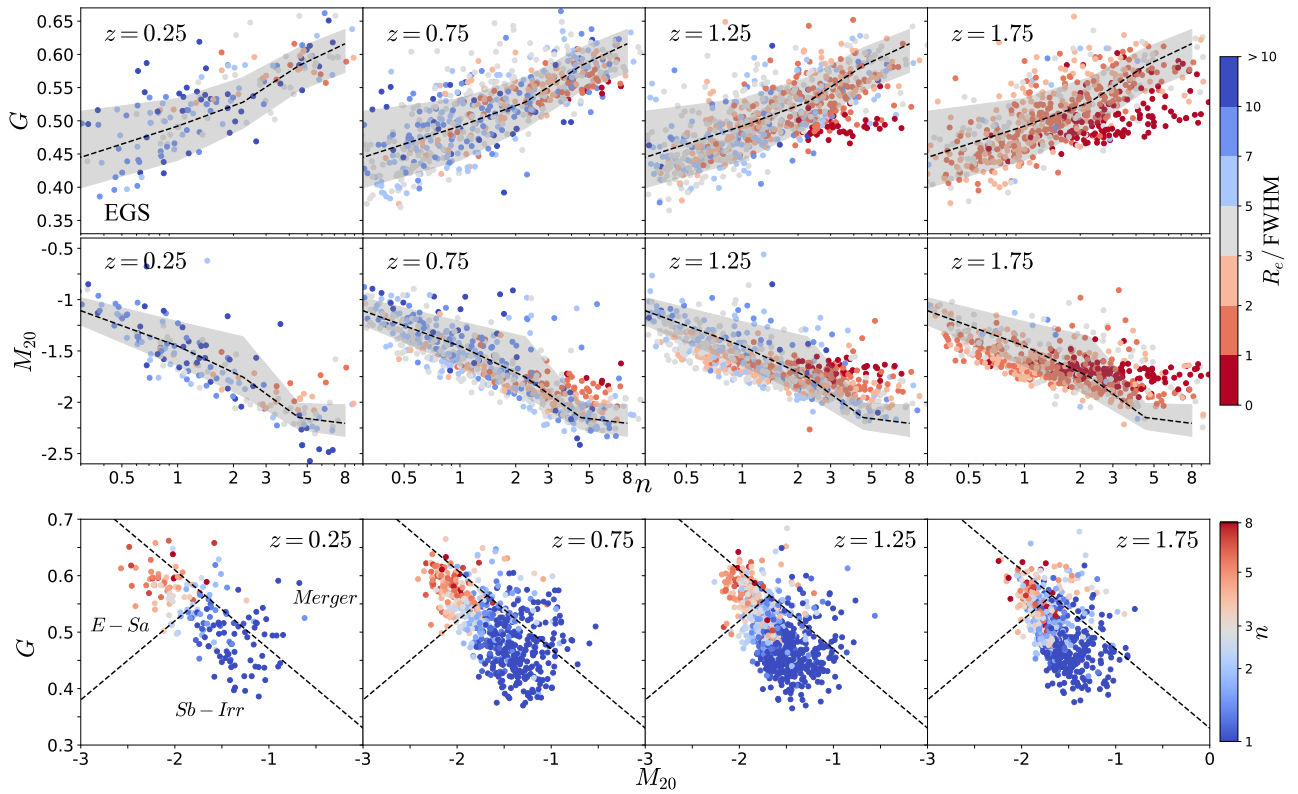


Fig. 11. The measured G (top row) and M_{20} (middle row) for the EGS images at $0 < z < 2$ as a function of n . In each panel, the black dashed line shows the median trend for the $R_e/\text{FWHM} > 5$ sub-samples at $z < 1$ (left two column), with the grey shaded region indicating the 16th to 84th percentile range of the variation. The distributions of galaxies in our sample at different redshift ranges in the G - M_{20} space are shown in the bottom row, colour-coded by the Sérsic index. The dashed lines are the boundaries between different galaxy types (Merger, E-Sa, Sb-Irr) derived from Lotz et al. (2008).

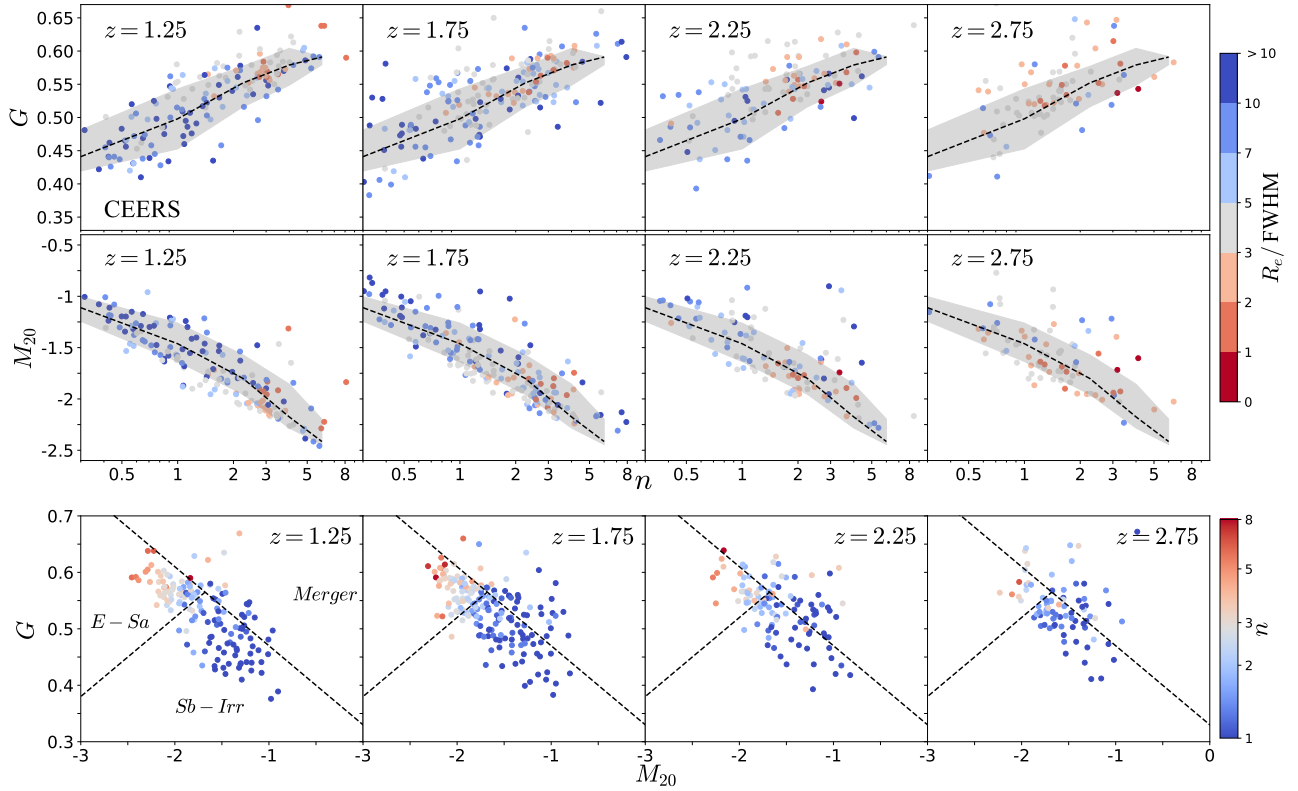


Fig. 12. Same as Fig. 11 but for the CEERS images at $1 < z < 3$. In each panel, the black dashed line shows the median trend for the $R_e/\text{FWHM} > 3$ sub-sample at $z = 1.25$ (left column), with the grey shaded region indicating the 16th to 84th percentile range of the variation. The parameters are less affected by the PSF smoothing effect. The E-Sa and Sb-Irr galaxies in the G - M_{20} are well separated in CEERS.

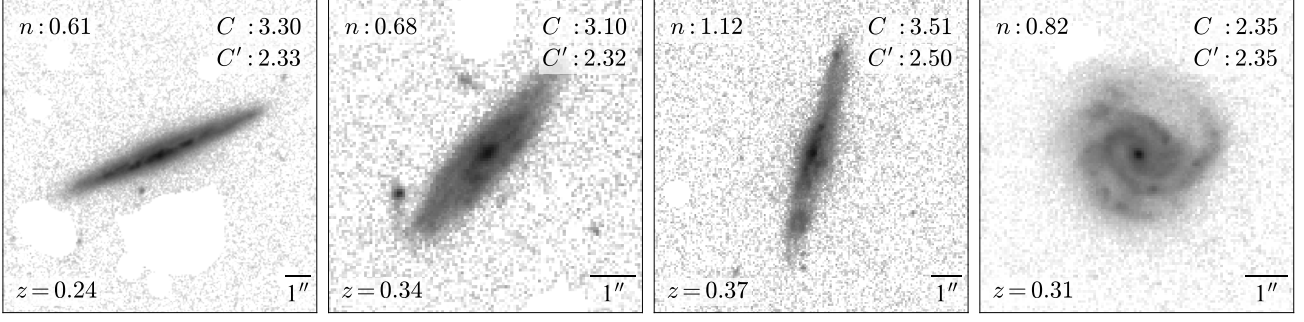


Fig. 13. Examples of the edge-on (left three panels) and face-on (right panel) galaxies at $z = 0.25$ for the EGS images. The left three edge-on galaxies with small axis ratio ($q < 0.3$) have C (from the circular aperture) overestimated compared to C' (from elliptical apertures with the same axis ratio as the galaxy outskirts). For the face-on galaxy, C and C' are close to each other.

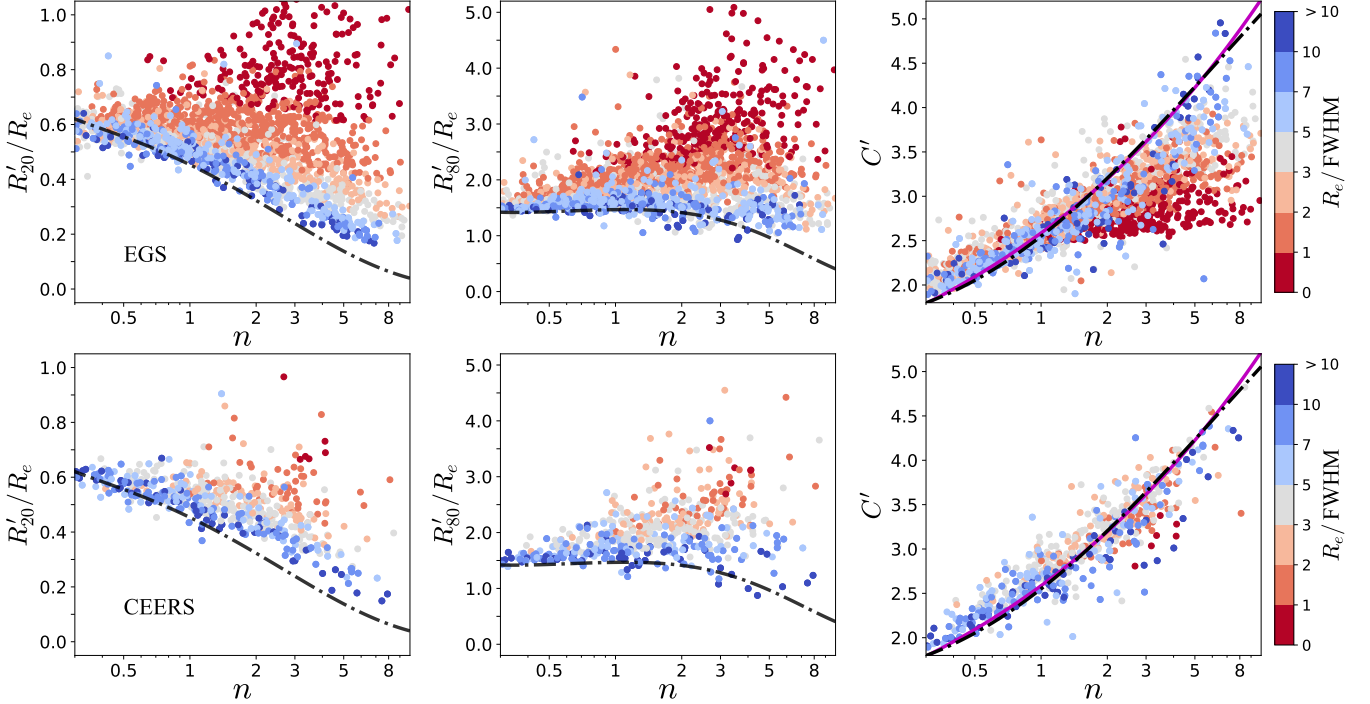


Fig. 14. Similar to Figs. 7 and 8, the structural parameters of all the EGS (top) and CEERS (bottom) images are measured with the elliptical apertures with the same axis ratio as the galaxy outskirts. The scatter is much more reduced compared to Figs. 7 and 8 for the galaxies with low n and large R_e/FWHM .

curate concentration index measurement to verify our previous result in Sect. 4.1.

The relationship between the measured C' and n is shown in Fig. 14. Compared to C , it is observed that most blue points ($R_e/\text{FWHM} > 5$) for C' align more closely with the expected correlation. The measured R'_{20}/R_e for the galaxies at small Sérsic indices with the elliptical apertures are slightly higher above the theoretical curve. This is mainly caused by the fact that the galaxy inner region is usually rounder than the outskirts due to the existence of the bulge (or AGN), with the PSF further enhancing this effect. Our test indicates that the axis ratio of the aperture is important to get the accurate concentration measurement, consistent with Andrae et al. (2011). Using the elliptical apertures can improve the accuracy of the concentration index measurement, as it prevents some edge-on galaxies from exhibiting higher C values in the case of the circular aperture. Nonetheless, our previous conclusions about the PSF smoothing effect

on the concentration index are not affected, as shown in the right column of Fig. 14.

5.2. Understanding the PSF smoothing effect with mock images

5.2.1. Test with the idealised mock images

To mimic the PSF smoothing effect on the galaxies in the F160W band with different sizes and Sérsic indices, we create a series of mock images on a 500×500 pixel grid with $0.5 \leq n \leq 8$ and $0.5 \leq R_e/\text{FWHM} \leq 15$ ($0.1'' \leq R_e \leq 3.0''$) with the pixel scale of $0.06''/\text{pixel}$, and the total magnitude $m = 18.5$ (with $S/N > 20$). These idealised images are measured with Statmorph for the non-parametric morphology indicators in the first place, then convolved with the PSF in F160W and added with the sky background in the same filter. The mock images are measured again Statmorph for the non-parametric morphology indicators, and compared with the intrinsic structural parameters.

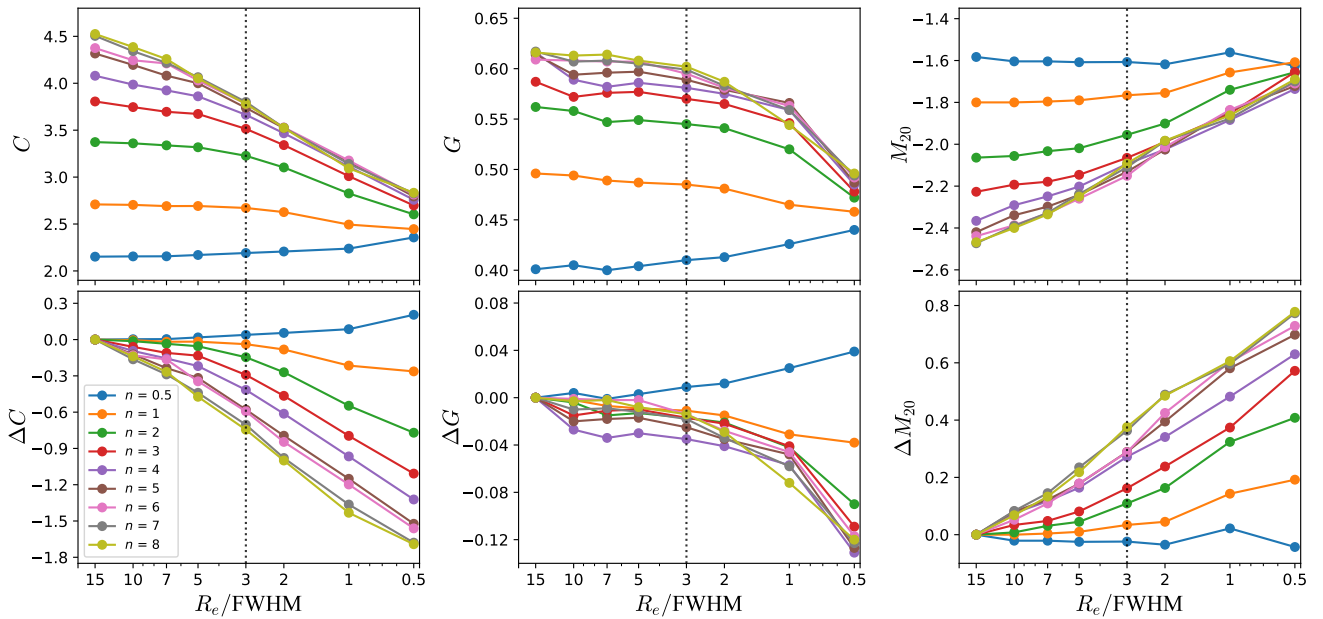


Fig. 15. The measured C (left), G (middle) and M_{20} (right) as a function of R_e/FWHM , with different colour representing different Sérsic indices. The top and bottom rows show the directly measured structural parameter (C , G , M_{20}) and the deviation from the intrinsic values (ΔC , ΔG , ΔM_{20}), respectively. As the galaxy becomes smaller, C , G and M_{20} gradually converge to the corresponding values of the PSF.

The variation of the measured C values with the galaxy sizes and Sérsic indices are shown in the top left panel of Fig. 15. The bottom left panel shows the relative deviation, $\Delta C = C - C_{\text{int}}$, where C_{int} is the intrinsic concentration index. It is clear that the C value remains roughly the same for low Sérsic indices ($n \leq 1$) with little or no impact from the PSF. For the galaxy with higher Sérsic index, as R_e/FWHM decreases, the concentration index estimated from the mock image decreases, with larger decrement for the galaxies of higher Sérsic indices.

The vertical dashed line marks the position at $R_e/\text{FWHM} = 3$, where the measured concentration indices of the mock images with $n \geq 4$ are roughly the same (~ 3.8). At even smaller R_e/FWHM , the C values of these mock images with high Sérsic indices (such as $n \geq 4$) are quite similar. This agrees with Andrae et al. (2011), that the C values of the galaxies with higher Sérsic indices are more affected than those with smaller Sérsic indices.

For the extremely small mock galaxies with different Sérsic indices and $R_e/\text{FWHM} \sim 0.5$, the C values converge to ~ 2.7 , corresponding to the value of the PSF. The results are in agreement with the C values of the smaller galaxies (red dots) in the bottom rows of Fig. 7. The concentration index directly measured from these images would be significantly underestimated, up to 30% for these small galaxies with high Sérsic indices ($n \geq 3$). This suggests that the galaxy light profile has been overshadowed by PSF. In other words, the measured C value does not reflect the shape of the galaxy light profile, but the shape of the PSF profile.

At different Sérsic indices, the G values roughly remain the same for the mock images with $R_e/\text{FWHM} \geq 3$, and then decrease at smaller R_e/FWHM , which eventually converge at ~ 0.5 . Note that at smaller R_e/FWHM , the measured G values of mock images with $n \sim 0.5$ actually increase to reach 0.5. Compared to the concentration index in the left column, the Gini coefficient measurement is less affected by the PSF smoothing effect. Moreover, for galaxies with $n > 3$, their G values are similar, with slightly larger G values for higher Sérsic indices. The

M_{20} statistic also shows the increasing pattern (with its absolute value decreasing) similar to the concentration index, which converges to ~ -1.70 .

The results of mock images for the CEERS F200W observation are shown in Appendix A, which are similar to the results of the EGS F160W mock images. Note that for extreme cases ($R_e/\text{FWHM} = 0.5$), R_e is only one pixel large. This galaxy can be considered as point source. The radial light profile actually reflects the PSF. However, in CEERS SW observations, it is rare to find $M_* > 10^{9.5} M_\odot$ galaxies with $R_e/\text{FWHM} < 1$ ($R_e \sim 0.06''$). In this case, these galaxies with higher n and smaller R_e do not show large deviation from the theoretical expectation between C and n .

5.2.2. Test with the artificially redshifted galaxies

To correct for the observational bias in the concentration-related parameters of the high redshift galaxies, the common approach is to create the mock images for the high redshift galaxies from the images of the low redshift ones, which are then measured to derive the corresponding correction factors (Giavalisco et al. 1996; Conselice 2003; Tohill et al. 2021; Yu et al. 2023). The basic procedure of the mock image generation includes resolution degradation, surface brightness dimming, size and luminosity evolution, PSF matching and noise addition. This strategy has been widely used to verify and correct the possible observational bias in the detection and measurement of bars and spiral arms in discs (van den Bergh et al. 2002; Sheth et al. 2008; Yu et al. 2018), the non-parametric indicators (Abraham et al. 1996; Petty et al. 2014; Whitney et al. 2021; Yu et al. 2023), the Sérsic index and size measurement of high redshift galaxies (Barden et al. 2008; Paulino-Afonso et al. 2017).

In order to evaluate the redshift effect, we also use the low redshift galaxies in the EGS images ($z \sim 0.3$) to generate the mock images of the HST observed higher redshift galaxies ($1.1 \leq z \leq 2.0$). Similar to Yu et al. (2023), first, we consider both the angular size variation of the galaxies at high red-

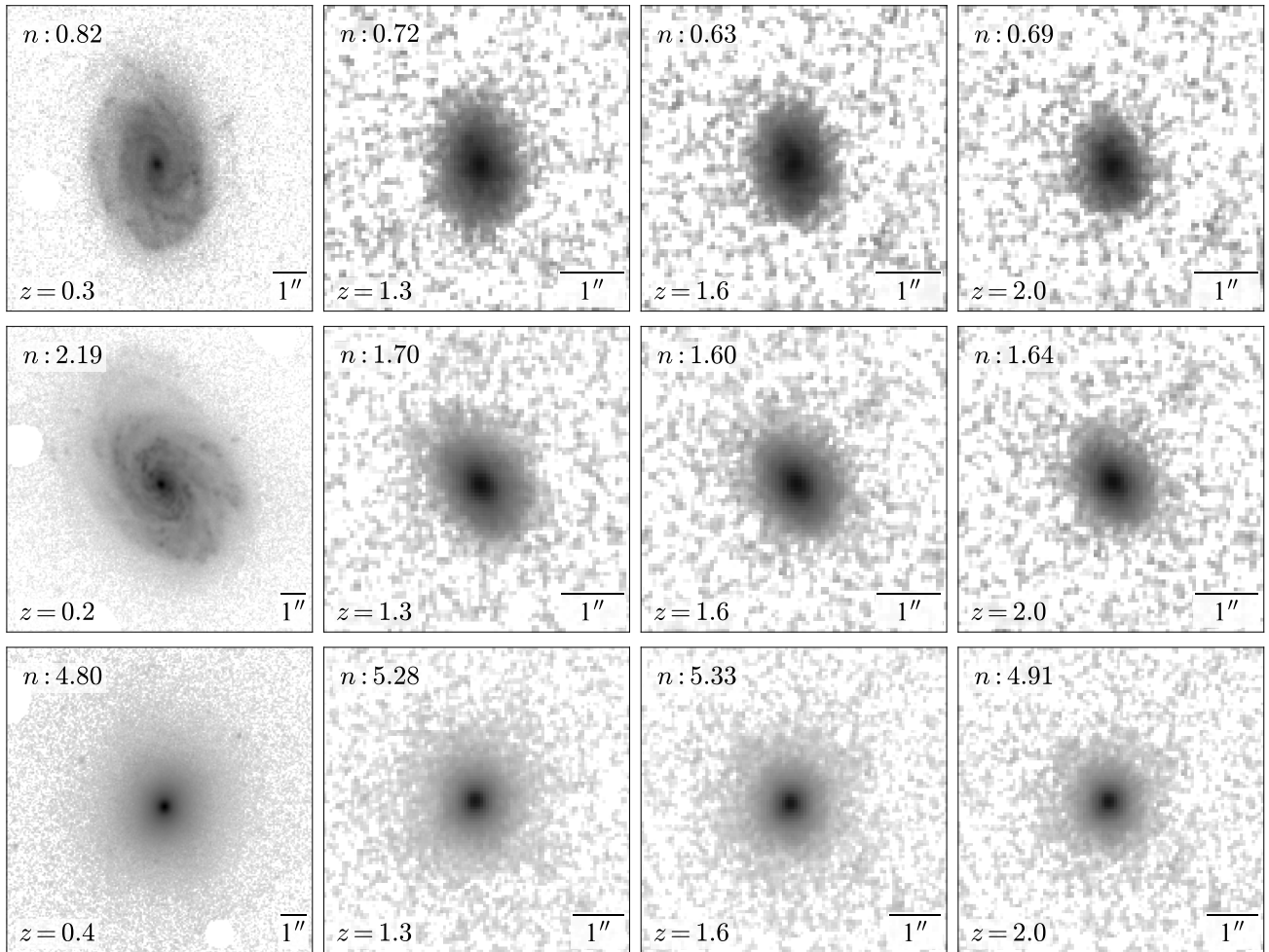


Fig. 16. Examples of the artificially redshifted galaxies in the HST observation. The original low redshift galaxy is shown in the left column, with the right three columns showing the high redshift mock images. The best-fit Sérsic index is also labelled in each panel.

shifts and size evolution through the cosmic time to re-scale the galaxy images with a proper rebinning factor. The evolution of the average effective radius is considered as $R_e \propto (1+z)^\beta$ with $\beta = -0.75$ for the discs and $\beta = -1.48$ for the spheroids (van der Wel et al. 2014). The discs and spheroids are separated at $n = 3$. The binned images are then scaled with $(1+z)^{-4}$ to account for the surface brightness dimming on the redshift (Tolman 1930) and $(1+z)$ for the cosmological compression of the frequency. We also adopt the luminosity evolution given by $(1+z)^\alpha$, where α is estimated for different rest-frame wavelengths, galaxy types, and stellar masses for the CANDELS galaxies (see Yu et al. (2023) for more details). The surface brightness (μ_f) for the mock galaxy at the final redshift (z_f) is

$$\mu_f = \mu_i + 2.5 \log \left(\frac{1+z_f}{1+z_i} \right)^3 - 2.5 \log \left(\frac{1+z_f}{1+z_i} \right)^\alpha - 2.5 \log \left(\frac{1+z_f}{1+z_i} \right)^{-2\beta} \quad (8)$$

where z_i and μ_i are the redshift and the surface brightness of the initial galaxy, respectively. We do not consider the morphological or magnitude k-correction, since our samples are at the similar rest-frame waveband, where the structural parameters do not vary too much (Conselice 2003; Baes et al. 2020; Nersesian et al. 2023). More details of these procedures are described in Appendix B.

In order to mimic the PSF effect, we rebin the original PSF in the filter at a lower redshift, similar to the galaxies binning procedure. Then we utilise the `create_matching_kernel` function in `Photutils` (Bradley et al. 2022) to create the PSF matching kernel. We choose the `TukeyWindow` to remove high frequency noise from the PSF matching kernel with

$$\sigma_{\text{kernel}} = \sqrt{\sigma_{\text{target}}^2 - \sigma_{\text{rebin}}^2},$$

where σ_{kernel} , σ_{target} and σ_{rebin} are the standard deviations of the PSF matching kernel, the target PSF and the rebinned PSF, respectively. Examples of mock images are shown in Fig. 16. Note that for the galaxies at $z = 1.1, 1.3,$ and 1.5 , the target PSF and the background are adopted from WFC3/F125W, while for the galaxies at $z = 1.6, 1.8,$ and 2.0 , the target PSF and the background are adopted from WFC3/F160W. We choose three typical galaxies with $n = 0.82, 2.19,$ and 4.80 to represent the morphological variation from the disc and the spheroid. At higher redshifts, the best-fit Sérsic index slightly reduces for the galaxies in the top and middle rows, but increases slightly for the galaxy in the bottom row.

Both mock images before and after the PSF convolution (with the sky background added) are both generated; the difference of the structural parameters between these two mock images can be used to quantify the PSF smoothing effect. We calculated the structural parameters for these mock galaxies (with

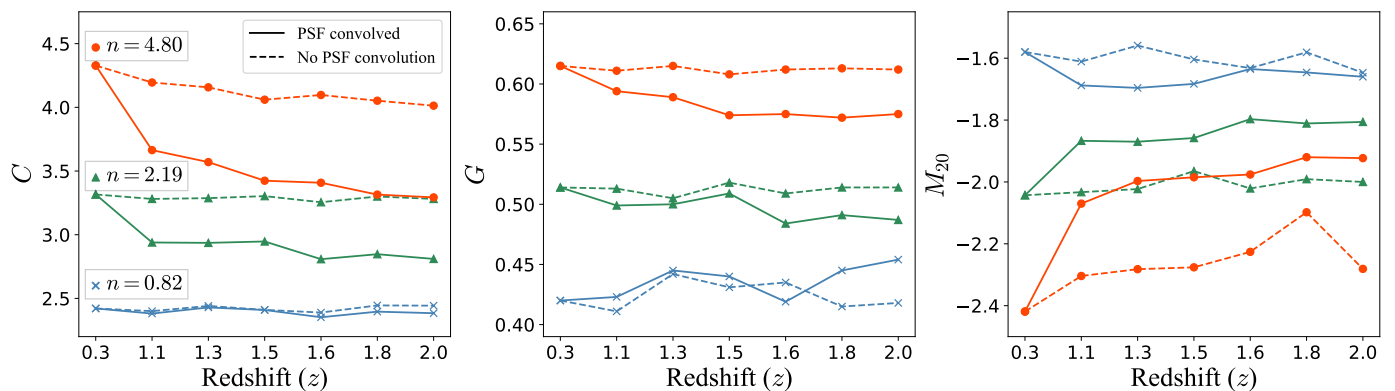


Fig. 17. The structural parameters of the three galaxies and the corresponding high redshift mock images in Fig. 16 are measured. The colour indicates the galaxies with different Sérsic indices ($n = 0.82, 2.19,$ and 4.80) for the top, middle, bottom rows in Fig. 16, respectively. The solid lines are the results of the PSF convolved mock galaxies, and the dashed lines are the results of the mock galaxies without the PSF convolution.

and without PSF convolution). Results of the C , G , and M_{20} are shown in the left, middle and right columns of Fig. 17, respectively. The solid and dashed lines are the results of the mock images with and without the PSF convolution, respectively. The non-parametric morphology indicators of the $n = 0.82$ galaxy (blue line) do not change much for the mock images with or without PSF convolution. While the Gini coefficient is lower at $z = 1.1$ and increases at the higher redshifts, primarily influenced by the noise. For the $n = 2.19$ galaxy (green line), the structural parameters of the images without the PSF convolution remain the same with increasing redshift, while the C , G and absolute value of M_{20} in the PSF convolved images decrease at higher redshift. For the $n = 4.80$ galaxy (red line) without the PSF convolution, the G value remains consistent across all redshifts, while the C and M_{20} values exhibit slight variations. At $z = 1.1$, the C value of the PSF convolved images decreases by 18% and then slightly reduces at higher redshifts. The G value and the absolute M_{20} decrease at $z = 1.1$ and remain unchanged at higher redshifts. Clearly, these structural parameters of the discs seem not sensitive to the PSF effect. While the structural parameters of the spheroids are significantly affected by the PSF, consistent with our previous results.

5.3. Comparison with previous works on the structural parameter measurement of high redshift galaxies

Whitney et al. (2021) investigated how the concentration and asymmetry indicators evolve using the CANDELS data. They artificially redshifted a sample of the low redshift galaxies ($0.5 < z < 1$) to different high redshift ranges (up to $z \sim 2.75$) to derive the corresponding correction factor for the structural parameters. They found that the higher redshift galaxies are more asymmetric and more concentrated. However, our tests indicate that the non-parametric indicators are affected differently by the PSF smoothing effect, depending on the Sérsic index and relative size of the galaxy. The C values of the galaxies with the higher Sérsic indices (spheroids) are usually more affected (underestimation) than the galaxies with the lower Sérsic indices (discs). For the galaxies with $n \leq 2$, the concentration index does not even need any correction. Without distinguishing different types of the galaxies (with different Sérsic indices), simply applying the same correction factor to all the measured C values of the high redshift galaxies would result in systematic overestimation of the intrinsic concentration index for discs and systematic underestimation for the spheroids at higher redshifts.

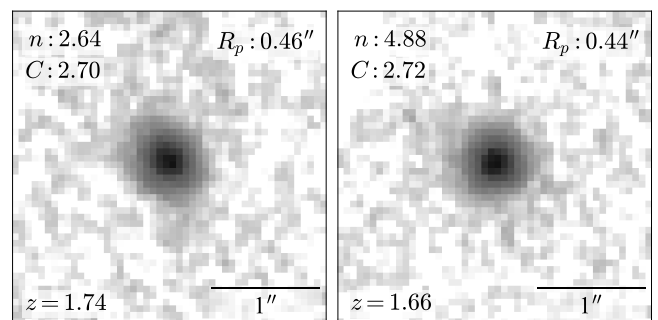


Fig. 18. Example of two galaxies in the EGS images at $z \sim 1.7$ with different n values, but similar C and R_p . Traditional correction method would not properly reflect the intrinsic difference in the light profile between the two galaxies.

Recently, Yu et al. (2023) utilised the high quality DESI images of the low redshift galaxies to create the mock images for the CEERS high redshift galaxies. They considered R_p/FWHM as an additional parameter for the correction, which is more accurate than the traditional methods. This correction works well at large R_p/FWHM , since the PSF smoothing effect is less severe. However, as shown in the left panel of Fig. 9 in their paper, the correction for small galaxies with $R_{p,\text{True}}/\text{FWHM} = 1.98$ still exhibits large scatter. This could only get worse for even smaller galaxies. For example, the two galaxies in EGS shown in Fig. 18 have similar R_p/FWHM and measured concentration values, but quite different intrinsic light profiles (i.e., the Sérsic index). The two galaxies would receive the same correction factor for C to produce incorrect values. Since JWST provides images with higher resolution than HST, most galaxies with $M_* > 10^{9.5} M_\odot$ in our sample have $R_p/\text{FWHM} > 5$ and the PSF smoothing effect is much weaker. The previous correction method is less useful for JWST SW images that do not even need any correction for the concentration index.

According to our results, the non-parametric method should be mainly used in conjunction with the model-dependent parameters, to ensure more robust measurement on the galaxy structural parameters. Note that the numerical relationship between C and n could not be simply adopted as the baseline of the correction for the concentration-related parameters, since the light profile of the real galaxy is usually too complicated to be accurately described by a single Sérsic model. For $R_e/\text{FWHM} \leq 3$

galaxies, the non-parametric method could not accurately reflect the light profile concentration. The traditional correction method without considering the light profile shape is unable to recover the true values. In fact, it is recommended to directly use the model-dependent parameters (R_e and n) from the 2D images modelling.

Yao et al. (2023) investigated the non-parametric morphology indicators of 1376 galaxies across the redshift ranges of $z \approx 0.8 - 3.0$ in the CEERS survey. Notice that no correction on the concentration index for high redshift galaxies was performed. Within this redshift range ($0.8 < z < 3$), the angular resolutions of the galaxy images are similar ($7.5-8.5$ kpc arcsec $^{-1}$). Moreover, they matched the PSF sizes across different wavelengths with the F200W PSF (FWHM $\sim 0.70''$) at the rest-frame optical wavelength, and with the F444W PSF (FWHM $\sim 0.14''$) at longer wavelength. They found that in the rest-frame optical wavelength bands, the measured C values of the massive galaxies ($M_* \geq 10^{10} M_\odot$) decrease with increasing redshift, and vice versa for low-mass galaxies. This result is different from Whitney et al. (2021) who adopted the correction for the concentration index. As Yao et al. (2023) has mentioned, such a difference may arise from the difference in the observational wavelength and the data processing procedures. In addition, according to our tests, matching the PSF of different filters to the lowest resolution would reduce the relative sizes of the galaxies (R_e/FWHM), resulting in inaccurate concentration-related parameters.

Recently, Kartaltepe et al. (2023) investigated the morphologies of 850 galaxies with $M_* > 10^9 M_\odot$ at $z = 3 - 9$ detected in both HST/WFC3 and CEERS JWST/NIRCam images. The empirical PSF FWHM of LW images are usually $\geq 0.12''$ (Finkelstein et al. 2023; Zhuang & Shen 2023), similar to the PSF FWHM of HST. In this case, the resolution of JWST detected $z > 3$ galaxies is comparable to that of HST detected $1 < z < 2$ galaxies at the rest-frame optical wavelength, as shown in Fig. 2 of Kartaltepe et al. (2023). In the left panel of Fig. 8 in their work, a significant fraction of the galaxies with higher Sérsic indices show lower C values ($C < 3$). According to our results, this phenomenon indicates severe PSF smoothing effect. The same issue may also exist in Ferreira et al. (2023), where the spheroids and discs with quite different Sérsic indices show very similar C values at different redshifts. About the galaxy morphological classification in the $G-M_{20}$ space, as shown in the right panel of Fig. 8 in Kartaltepe et al. (2023), the Sérsic indices of some galaxies in the E-Sa and merger regions are large, consistent with our results. This alignment confirms that the G and M_{20} parameters are also affected by the PSF smoothing effect, but to a less extent than C .

The higher redshift galaxies are substantially more compact with smaller R_e than the lower redshift counterparts (Daddi et al. 2005; Cassata et al. 2013; van der Wel et al. 2014), which should naturally be more affected by PSF to exhibit lower C values, especially for those with higher Sérsic indices. For the $z > 3$ galaxies observed by JWST in LW, the PSF smoothing effect on the non-parametric indicators is also significant, and the model dependent method should be considered.

5.4. Comparison between JWST and HST structural parameters

Kartaltepe et al. (2023) and Ferreira et al. (2023) have compared the morphologies of the same galaxies in both HST and JWST observations. Some galaxies exhibit the distinct spiral structures in JWST images that are not as pronounced as the HST images, potentially leading to misinterpretation as mergers in the HST

observations. In addition, many high redshift galaxies previously identified as spheroids in HST are later confirmed as discs in JWST observations. So the structural parameters between JWST and HST observations are expected to be different.

In the comparison of the structural parameters for galaxies observed by both HST and JWST at the rest-frame optical wavelength (Fig. 19), we find that at lower concentrations (and smaller Sérsic indices), C_{HST} and C_{JWST} (top left panel) are in agreement. However, for galaxies with higher Sérsic indices, C_{JWST} tends to be larger than C_{HST} . C_{59} (bottom left panel), G (top middle panel) show similar pattern as the concentration index but with less scatter. Compared to the JWST results, $M_{20,\text{HST}}$ (bottom middle panel) is overestimated at lower values while underestimated at higher values. This maybe due to the fact that M_{20} is more sensitive to the resolution of images, not only for spheroids, but also for discs (though C , G and n for discs are less affected by the systematic effects). The Sérsic indices for both HST and JWST observations are consistent but exhibiting a large scatter at higher n values. The effective radii (R_e) are well aligned with each other. This confirms that the 2D image modelling of the HST galaxy images can produce robust Sérsic index and size measurement consistent with the JWST observations.

5.5. The evolution of galaxy structural parameters

Here we investigate the evolution of the galaxy light profiles for low-mass ($10^{9.5} M_\odot \leq M_* < 10^{10.5} M_\odot$) and high-mass ($10^{10.5} M_\odot \leq M_* < 10^{11.5} M_\odot$) galaxies in our sample. We mainly focus on the Sérsic index and the effective radius derived by fitting the single Sérsic model to the galaxy mosaic with GALFIT. As shown in Fig. 20, both mass sub-samples follow similar decreasing trend of galaxy size (R_e) with increasing redshift. In certain redshift ranges, the typical sizes of the high-mass and low-mass galaxies are similar. The Sérsic index of low-mass galaxies are ~ 1 at different redshift ranges. For the high-mass galaxies, the Sérsic index decreases from $n \sim 4$ at lower redshifts to ~ 3 at higher redshifts. Our result confirms that galaxies at higher redshifts are more compact with smaller R_e (e.g. Daddi et al. 2005; Trujillo et al. 2007; Buitrago et al. 2008; van Dokkum et al. 2010; Weinzirl et al. 2011; Barro et al. 2013; Williams et al. 2014; van der Wel et al. 2014; Davari et al. 2017). In addition, higher mass galaxies at $z < 1$ have larger Sérsic indices, due to a high fraction of spheroids present at lower redshifts in our sample. While for lower mass galaxies, the Sérsic indices at each redshift bin is roughly the same ($n \sim 1$), suggesting the prevalence of discs in these lower mass systems.

When describing the galaxy light distribution, it is important to distinguish between ‘concentrated’ and ‘compact’. The former implies that most of the galaxy’s flux is centrally distributed, while the latter implies a smaller size and higher density. Our results, along with the findings from Yao et al. (2023), suggest that high-mass galaxies at higher redshifts are less concentrated compared to those at lower redshifts, but they appear more compact. Various mechanisms, such as an inside-out formation process could contribute to this phenomenon. In the future, more space based large scale surveys (CSST, Euclid, Roman) will help to answer this question of galaxy growth and structure evolution.

6. Conclusion

In this work, we investigate the PSF smoothing effect on the concentration-related structural parameters (C , G , M_{20}) in observations and mock images. We select a mass-limited sample ($10^{9.5} M_\odot \leq M_* \leq 10^{11.5} M_\odot$) of 2305 galaxies at redshift

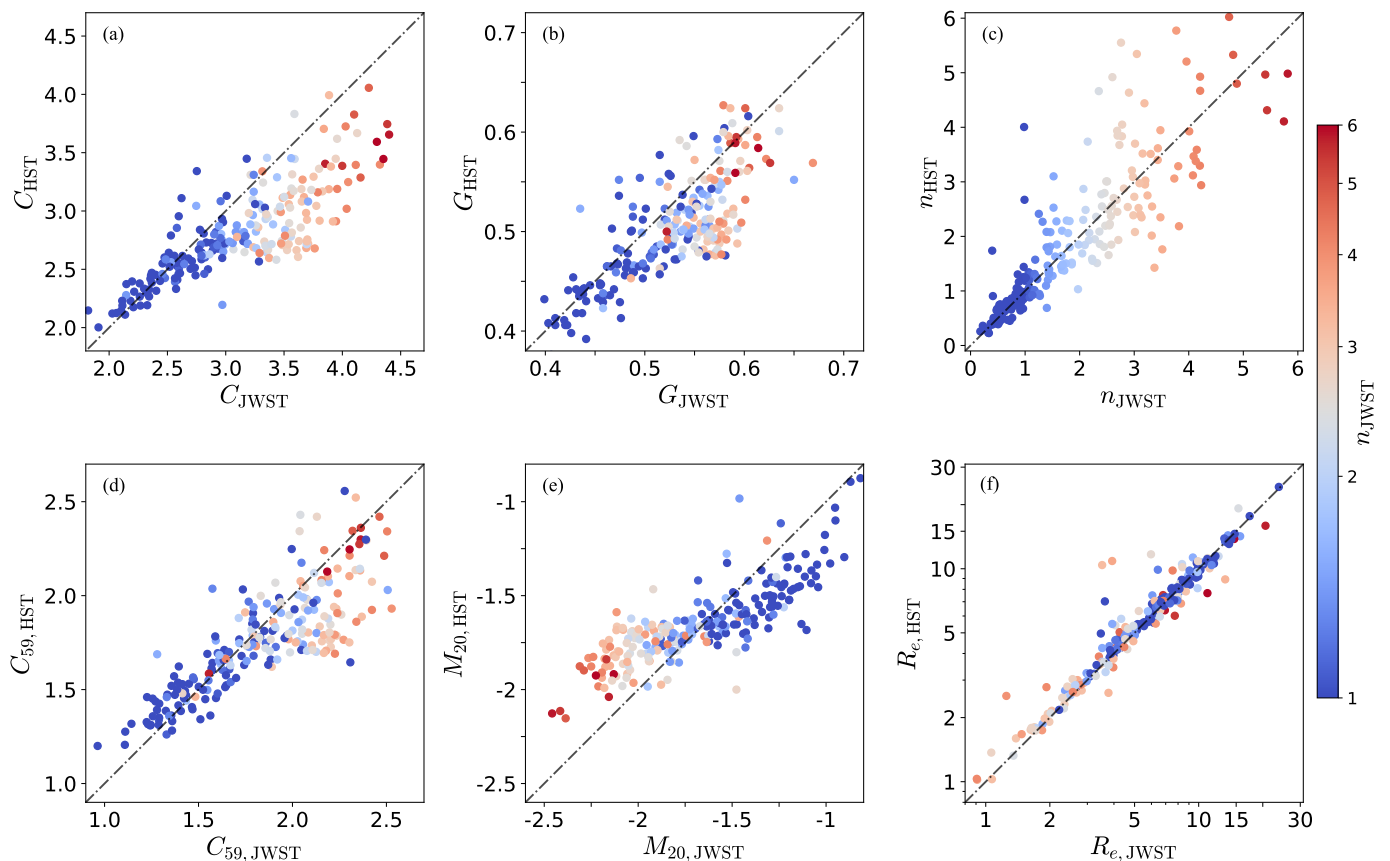


Fig. 19. Comparison of the structural parameters of the galaxies in our sample both observed by the JWST (X-axis) and HST (Y-axis) at the rest-frame optical wavelength, colour-coded by n_{JWST} measured from the CEERS images.

$0 < z < 2$ from the EGS field in the CANDELS survey and 524 galaxies at $1 < z < 3$ from the CEERS survey. The images in different filters are used for different redshift ranges to ensure similar rest-frame optical wavelength. It has been shown that the Sérsic index can be robustly derived from 2D image fitting with PSF convolution, therefore it can be used as a reliable indicator for the intrinsic shape of the light profile. To understand the PSF smoothing effect on the non-parametric morphology indicators for high redshift galaxies, we investigate the dependence of the non-parametric morphology indicators on the Sérsic index and the relative size of the galaxy (R_e/FWHM) with HST and JWST observations, and mock images.

Our conclusions are listed as follows.

1. The concentration index is generally underestimated due to the PSF smoothing effect, especially for the smaller galaxies with higher Sérsic index. For the galaxies with lower Sérsic index ($n \leq 2$) or larger relative size ($R_e/\text{FWHM} > 3$), the concentration index is almost unaffected. With the idealised mock images, we confirm that the underestimation of the C value is mainly due to the more significant overestimation of R_{20}/R_e (compared to R_{80}/R_e). Another commonly used concentration index C_{59} (derived from R_{90} and R_{50}) is less affected by the PSF smoothing effect, except for the smaller galaxies with $R_e/\text{FWHM} < 1$. The correlation between C_{59} and n is relatively weaker (with larger scatter) than that between C and n .
2. The Gini coefficient is less affected by the PSF smoothing effect, while the absolute value of M_{20} is underestimated, in a similar fashion to the C -value. For the galaxies observed

by HST, the empirical morphological classification in the G - M_{20} space works well at lower redshifts, but fails at higher redshifts, with the discs and spheroids mixed together. However, for the galaxies observed by JWST at $1 < z < 3$, the empirical separation between the E-Sa and Sb-Irr galaxies in the G - M_{20} space works well.

3. We discuss the influence of the axis ratio of the aperture used in the concentration index measurement. With the traditional circular aperture, the C values of the edge-on discs are overestimated to deviate from the theoretical expectation between the C and n parameters. When adopting the elliptical apertures with the same ellipticity as the galaxy outskirts, the correlation between C and n is significantly improved to show much tighter correlation. Our main conclusions are not affected by the different aperture shapes.
4. The traditional correction method for the non-parametric morphology indicators may not be accurate enough. Both the relative size of the galaxy (R_e/FWHM) and the Sérsic index play important roles here. In fact, the Sérsic index is a better choice to represent the light concentration for these high redshift galaxies.
5. According to the structural parameters measured with single Sérsic component fitting, we confirm that the galaxies at higher redshifts are more compact with smaller R_e . At different redshifts, the lower mass galaxies have Sérsic index $n \sim 1$ (disc dominated). For higher mass galaxies, the Sérsic index decrease from ~ 4 to ~ 3 at higher redshifts.

Acknowledgements. We thank the referee for the helpful comments to improve the paper and Iulia Simion for polishing the language. This work is supported by the National Natural Science Foundation of China under grant No. 12122301,

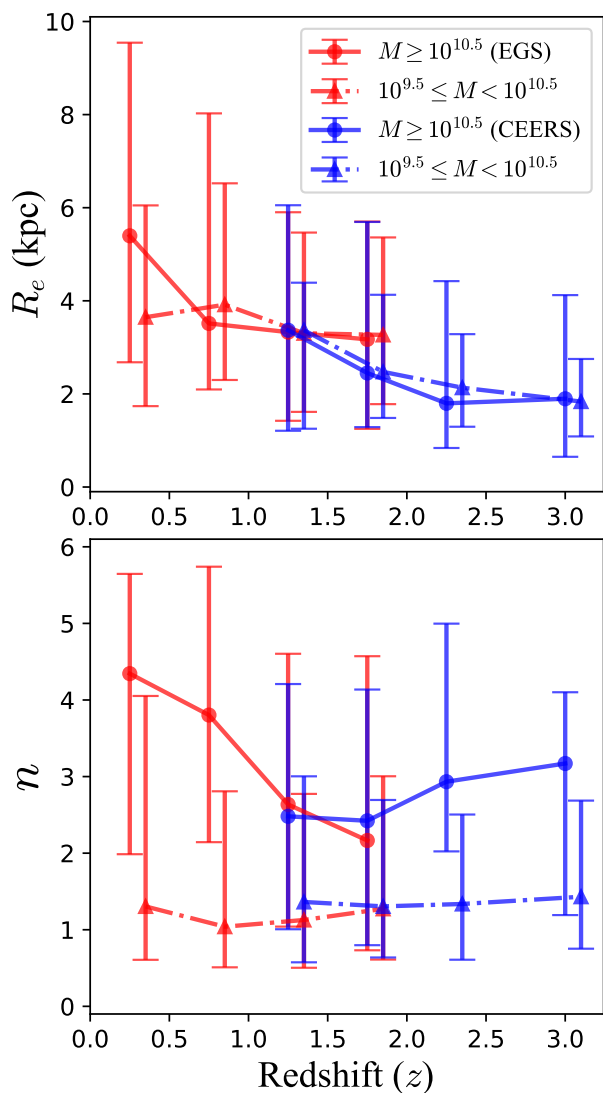


Fig. 20. Evolution of the effective radius (top) and Sérsic index (bottom) for galaxies in our sample. The triangle with dashed solid lines are the median values for low-mass galaxies ($10^{9.5}M_{\odot} \leq M_* < 10^{10.5}M_{\odot}$), while the circles with solid lines are the means for high-mass galaxies ($M_* \geq 10^{10.5}M_{\odot}$). Error bars define the 16th and 84th percentiles of the distributions. The EGS and CEERS images are colour-coded by the red and blue lines, respectively.

12233001, by a Shanghai Natural Science Research Grant (21ZR1430600), by the “111” project of the Ministry of Education under grant No. B20019, and by the China Manned Space Project with No. CMS-CSST-2021-A04. We thank the sponsorship from Yangyang Development Fund. This work made use of the Gravity Supercomputer at the Department of Astronomy, Shanghai Jiao Tong University. LCH was supported by the National Science Foundation of China (11721303, 11991052, 12011540375, 12233001), the National Key R&D Program of China (2022YFF0503401), and the China Manned Space Project (CMS-CSST-2021-A04, CMS-CSST-2021-A06). This work has made use of the Rainbow Cosmological Surveys Database, which is operated by the Centro de Astrobiología (CAB/INTA), partnered with the University of California Observatories at Santa Cruz (UCO/Lick,UCSC).

References

Abraham, R. G., van den Bergh, S., Glazebrook, K., et al. 1996, *ApJS*, 107, 1
 Abraham, R. G., van den Bergh, S., & Nair, P. 2003, *ApJ*, 588, 218
 Allen, R. J., Kacprzak, G. G., Glazebrook, K., et al. 2017, *ApJ*, 834, L11
 Andrae, R., Jahnke, K., & Melchior, P. 2011, *MNRAS*, 411, 385

Astropy Collaboration, Price-Whelan, A. M., Lim, P. L., et al. 2022, *ApJ*, 935, 167
 Baes, M., Nersesian, A., Casasola, V., et al. 2020, *A&A*, 641, A119
 Bagley, M. B., Finkelstein, S. L., Koekemoer, A. M., et al. 2023, *ApJ*, 946, L12
 Barden, M., Häußler, B., Peng, C. Y., McIntosh, D. H., & Guo, Y. 2012, *MNRAS*, 422, 449
 Barden, M., Jahnke, K., & Häußler, B. 2008, *ApJS*, 175, 105
 Barro, G., Faber, S. M., Pérez-González, P. G., et al. 2013, *ApJ*, 765, 104
 Bertin, E. 2011, in *Astronomical Society of the Pacific Conference Series*, Vol. 442, *Astronomical Data Analysis Software and Systems XX*, ed. I. N. Evans, A. Accomazzi, D. J. Mink, & A. H. Rots, 435
 Bertin, E. & Arnouts, S. 1996, *A&AS*, 117, 393
 Blanton, M. R., Dalcanton, J., Eisenstein, D., et al. 2001, *AJ*, 121, 2358
 Bottrell, C., Simard, L., Mendel, J. T., & Ellison, S. L. 2019, *MNRAS*, 486, 390
 Bradley, L., Sipőcz, B., Robitaille, T., et al. 2022, *astropy/photutils: 1.5.0*
 Bruce, V. A., Dunlop, J. S., McLure, R. J., et al. 2014, *MNRAS*, 444, 1001
 Buitrago, F., Trujillo, I., Conselice, C. J., et al. 2008, *ApJ*, 687, L61
 Caon, N., Capaccioli, M., & D’Onofrio, M. 1993, *MNRAS*, 265, 1013
 Cassata, P., Giavalisco, M., Williams, C. C., et al. 2013, *ApJ*, 775, 106
 Conselice, C. J. 2003, *ApJS*, 147, 1
 Conselice, C. J., Bershady, M. A., & Jangren, A. 2000, *ApJ*, 529, 886
 Conselice, C. J., Bluck, A. F. L., Mortlock, A., Palamara, D., & Benson, A. J. 2014, *MNRAS*, 444, 1125
 Conselice, C. J., Rajgor, S., & Myers, R. 2008, *MNRAS*, 386, 909
 Daddi, E., Renzini, A., Pirzkal, N., et al. 2005, *ApJ*, 626, 680
 Davari, R., Ho, L. C., Peng, C. Y., & Huang, S. 2014, *ApJ*, 787, 69
 Davari, R. H., Ho, L. C., Mobasher, B., & Canalizo, G. 2017, *ApJ*, 836, 75
 de Souza, R. E., Gadotti, D. A., & dos Anjos, S. 2004, *ApJS*, 153, 411
 Erwin, P. 2015, *ApJ*, 799, 226
 Ferreira, L., Conselice, C. J., Sazonova, E., et al. 2023, *ApJ*, 955, 94
 Finkelstein, S. L., Bagley, M. B., Ferguson, H. C., et al. 2023, *ApJ*, 946, L13
 Freeman, K. C. 1970, *ApJ*, 160, 811
 Gadotti, D. A. 2008, *MNRAS*, 384, 420
 Gadotti, D. A. 2009, *MNRAS*, 393, 1531
 Gao, H., Ho, L. C., Barth, A. J., & Li, Z.-Y. 2018, *ApJ*, 862, 100
 Gao, H., Ho, L. C., Barth, A. J., & Li, Z.-Y. 2020, *ApJS*, 247, 20
 Giavalisco, M., Livio, M., Bohlin, R. C., Macchetto, F. D., & Stecher, T. P. 1996, *AJ*, 112, 369
 Glasser, G. J. 1962, *Journal of the American Statistical Association*, 57, 648
 Graham, A. W., Driver, S. P., Petrosian, V., et al. 2005, *AJ*, 130, 1535
 Grogin, N. A., Kocevski, D. D., Faber, S. M., et al. 2011, *ApJS*, 197, 35
 Gunn, J. E. & Gott, J. Richard, I. 1972, *ApJ*, 176, 1
 Hubble, E. P. 1926, *ApJ*, 64, 321
 Huertas-Company, M., Bernardi, M., Pérez-González, P. G., et al. 2016, *MNRAS*, 462, 4495
 Kartaltepe, J. S., Rose, C., Vanderhoof, B. N., et al. 2023, *ApJ*, 946, L15
 Kauffmann, G., Heckman, T. M., White, S. D. M., et al. 2003, *MNRAS*, 341, 33
 Kent, S. M. 1985, *ApJS*, 59, 115
 Koekemoer, A. M., Faber, S. M., Ferguson, H. C., et al. 2011, *ApJS*, 197, 36
 Kormendy, J. 1977a, *ApJ*, 218, 333
 Kormendy, J. 1977b, *ApJ*, 217, 406
 Kormendy, J. & Bender, R. 2012, *ApJS*, 198, 2
 Kormendy, J. & Kennicutt, Robert C., J. 2004, *ARA&A*, 42, 603
 Kron, R. G. 1980, *ApJS*, 43, 305
 Larson, R. B., Tinsley, B. M., & Caldwell, C. N. 1980, *ApJ*, 237, 692
 Laurikainen, E., Salo, H., & Buta, R. 2005, *MNRAS*, 362, 1319
 Lintott, C., Schawinski, K., Bamford, S., et al. 2011, *MNRAS*, 410, 166
 Lisker, T. 2008, *ApJS*, 179, 319
 López-Sanjuan, C., Balcells, M., Pérez-González, P. G., et al. 2009, *A&A*, 501, 505
 Lotz, J. M., Davis, M., Faber, S. M., et al. 2008, *ApJ*, 672, 177
 Lotz, J. M., Primack, J., & Madau, P. 2004, *AJ*, 128, 163
 Meert, A., Vikram, V., & Bernardi, M. 2015, *MNRAS*, 446, 3943
 Méndez-Abreu, J., Ruiz-Lara, T., Sánchez-Menguiano, L., et al. 2017, *A&A*, 598, A32
 Moore, B., Katz, N., Lake, G., Dressler, A., & Oemler, A. 1996, *Nature*, 379, 613
 Mortlock, A., Conselice, C. J., Hartley, W. G., et al. 2013, *MNRAS*, 433, 1185
 Nersesian, A., Zibetti, S., D’Eugenio, F., & Baes, M. 2023, *A&A*, 673, A63
 Paulino-Afonso, A., Sobral, D., Buitrago, F., & Afonso, J. 2017, *MNRAS*, 465, 2717
 Peng, C. Y., Ho, L. C., Impey, C. D., & Rix, H.-W. 2002, *AJ*, 124, 266
 Peng, C. Y., Ho, L. C., Impey, C. D., & Rix, H.-W. 2010, *AJ*, 139, 2097
 Petrosian, V. 1976, *ApJ*, 210, L53
 Petty, S. M., Armus, L., Charmandaris, V., et al. 2014, *AJ*, 148, 111
 Rodríguez-Gomez, V., Snyder, G. F., Lotz, J. M., et al. 2019, *MNRAS*, 483, 4140
 Sandage, A. 2005, *ARA&A*, 43, 581
 Sérsic, J. L. 1968, *Atlas de Galaxias Australes*
 Sheth, K., Elmegreen, D. M., Elmegreen, B. G., et al. 2008, *ApJ*, 675, 1141

- Simard, L., Mendel, J. T., Patton, D. R., Ellison, S. L., & McConnell, A. W. 2011, *ApJS*, 196, 11
- Simard, L., Willmer, C. N. A., Vogt, N. P., et al. 2002, *ApJS*, 142, 1
- Simien, F. & de Vaucouleurs, G. 1986, *ApJ*, 302, 564
- Stefanon, M., Yan, H., Mobasher, B., et al. 2017, *ApJS*, 229, 32
- Strateva, I., Ivezić, Ž., Knapp, G. R., et al. 2001, *AJ*, 122, 1861
- Sun, W., Ho, L. C., Zhuang, M.-Y., et al. 2023, arXiv e-prints, arXiv:2308.09076
- Tohill, C., Ferreira, L., Conselice, C. J., Bamford, S. P., & Ferrari, F. 2021, *ApJ*, 916, 4
- Tolman, R. C. 1930, *Proceedings of the National Academy of Sciences*, 16, 511
- Trujillo, I., Conselice, C. J., Bundy, K., et al. 2007, *MNRAS*, 382, 109
- Trujillo, I., Graham, A. W., & Caon, N. 2001, *MNRAS*, 326, 869
- van den Bergh, S., Abraham, R. G., Whyte, L. F., et al. 2002, *AJ*, 123, 2913
- van der Wel, A., Bell, E. F., Häussler, B., et al. 2012, *ApJS*, 203, 24
- van der Wel, A., Franx, M., van Dokkum, P. G., et al. 2014, *ApJ*, 788, 28
- van Dokkum, P. G., Whitaker, K. E., Brammer, G., et al. 2010, *ApJ*, 709, 1018
- Weinzirl, T., Jogee, S., Conselice, C. J., et al. 2011, *ApJ*, 743, 87
- White, S. D. M. & Rees, M. J. 1978, *MNRAS*, 183, 341
- Whitney, A., Conselice, C. J., Bhatwadekar, R., & Duncan, K. 2019, *ApJ*, 887, 113
- Whitney, A., Conselice, C. J., Duncan, K., & Spitler, L. R. 2020, *ApJ*, 903, 14
- Whitney, A., Ferreira, L., Conselice, C. J., & Duncan, K. 2021, *ApJ*, 919, 139
- Williams, C. C., Giavalisco, M., Cassata, P., et al. 2014, *ApJ*, 780, 1
- Yao, Y., Song, J., Kong, X., et al. 2023, *ApJ*, 954, 113
- Yesuf, H. M., Ho, L. C., & Faber, S. M. 2021, *ApJ*, 923, 205
- Yu, S.-Y., Cheng, C., Pan, Y., Sun, F., & Li, Y. A. 2023, *A&A*, 676, A74
- Yu, S.-Y., Ho, L. C., Barth, A. J., & Li, Z.-Y. 2018, *ApJ*, 862, 13
- Zhuang, M.-Y. & Shen, Y. 2023, arXiv e-prints, arXiv:2304.13776

Appendix A: Idealised mock images for JWST

Similar to the generation of idealised mock galaxies for the EGS F160W images in Sect. 5.2.1, we create a series of mock images on a 500×500 pixel grid with $0.5 \leq n \leq 8$ and $0.5 \leq R_e/\text{FWHM} \leq 15$ ($0.035'' \leq R_e \leq 1.05''$) at a total magnitude of $m = 21$ (with $S/N > 20$). These images are then convolved with the NIRCcam/F200W band PSF and added to the sky background in the same filter. The mock images are measured using Statmorph to extract the non-parametric morphology indicators. The impact of the PSF on C , G and M_{20} is shown in Fig. A.1. The top rows show the variation of indicators with different R_e/FWHM for different Sérsic profiles, and the bottom rows show the relative deviation. The trend of decreasing R_e/FWHM is consistent with the result of the EGS Sérsic mock galaxies. When the PSF FWHM is larger than the R_e ($R_e/\text{FWHM} = 0.5$), the C values converge to ~ 3.5 for all galaxies. However, for $n = 0.5$ cases, the G values increase rapidly as R_e/FWHM decreased and converge to ~ 0.5 , close to the results of higher n objects. This behaviour may be attributed to the small FWHM of the PSF from the NIRCcam detector, providing higher quality images.

Appendix B: The procedures of artificially redshifted galaxies

The steps for artificially redshifted galaxies have been outlined in previous studies (Giavalisco et al. 1996; Conselice 2003; Bardeen et al. 2008; Yu et al. 2023). Following their methods, these steps are listed below. e

1. Compute rebinning factor and rebin images

The physical size of a galaxy will remain at higher redshift, so its angular size a_f can be calculated from initial redshift z_i to final redshift z_f

$$D_{A,i}a_i = D_{A,f}a_f, \quad (\text{B.1})$$

$$\frac{D_{L,i}a_i}{(1+z_i)^2} = \frac{D_{L,f}a_f}{(1+z_f)^2}, \quad (\text{B.2})$$

where D_A and D_L are angular distance and luminosity distance at objective redshift respectively. When simulating initial imaging surveys with a pixel scale of p_i transitioning to a target pixel scale of p_f , the rebinning factor is given by

$$B = \frac{a_i/p_i}{a_f/p_f} = \frac{p_f D_{L,f}}{p_i D_{L,i}} \frac{(1+z_i)^2}{(1+z_f)^2}. \quad (\text{B.3})$$

Here, the small angle approximation $\tan(a) \sim a$ is employed. We also consider the size evolution of galaxies given by $R_e \propto (1+z)^\beta$ (van der Wel et al. 2014), then the rebinning factor becomes

$$B = \frac{p_f D_{L,f}}{p_i D_{L,i}} \cdot \frac{(1+z_i)^2}{(1+z_f)^2} \cdot \frac{(1+z_i)^{-\beta}}{(1+z_f)^{-\beta}}, \quad (\text{B.4})$$

2. Rescale the flux

If the bolometric luminosity of the galaxy remains constant when shifting to different redshifts, we have

$$4\pi D_{L,i}^2 f_i = 4\pi D_{L,f}^2 f_f. \quad (\text{B.5})$$

Here, f_i and f_f are the observed fluxes at z_i and z_f . The ratio of the flux density per unit solid angle between z_i and z_f is then given by:

$$\frac{f_f/a_f^2}{f_i/a_i^2} = \frac{D_{L,i}^2}{D_{L,f}^2} \cdot \frac{a_i^2}{a_f^2} = \frac{(1+z_i)^4}{(1+z_f)^4}, \quad (\text{B.6})$$

resulting in the standard surface brightness dependence of $(1+z)^{-4}$ (Tolman 1930). A filter has central wavelength λ and width $\Delta\lambda$. Both the observed central wavelength and the observed bandwidth increase by a factor of $(1+z)$. In units of $\text{erg s}^{-1}\text{cm}^{-2}\text{Hz}^{-1}$, the surface brightness scales as $\mu \propto (1+z)^{-3}$. Consider the luminosity evolution given by $(1+z)^\alpha$ (Yu et al. 2023), the final apparent magnitude (M_f) is

$$M_f = M_i + 2.5\log\left(\frac{1+z_f}{1+z_i}\right)^3 - 2.5\log\left(\frac{1+z_f}{1+z_i}\right)^\alpha. \quad (\text{B.7})$$

So the final surface brightness (μ_f) becomes

$$\begin{aligned} \mu_f &= \mu_i + 2.5\log\left(\frac{1+z_f}{1+z_i}\right)^3 \\ &\quad - 2.5\log\left(\frac{1+z_f}{1+z_i}\right)^\alpha - 2.5\log\left(\frac{1+z_f}{1+z_i}\right)^{-2\beta}. \end{aligned} \quad (\text{B.8})$$

The morphological or magnitude k-correction is ignored, since our samples are at the rest-frame optical waveband.

3. PSF convolution

In order to mimic the PSF effect, we rebin the original PSF in the filter at lower redshift, similar to the galaxies rebinning procedure. Then we utilise the `create_matching_kernel` function in Photutils (Bradley et al. 2022) to create the PSF matching kernel κ , following

$$\text{PSF}_i(x, y) \otimes \kappa(x, y) = \text{PSF}_f(x, y), \quad (\text{B.9})$$

$$\kappa(x, y) = F^{-1}\left(\frac{F(\text{PSF}_f(x, y))}{F(\text{PSF}_i(x, y))}\right), \quad (\text{B.10})$$

where \otimes is the convolution operator, and F (F^{-1}) is (inverse) Fourier transformation operator. We choose the TukeyWindow to remove high frequency noise from the PSF matching kernel with

$$\sigma_\kappa = \sqrt{\sigma_f^2 - \sigma_i^2}, \quad (\text{B.11})$$

where σ_κ , σ_f and σ_i are the stand deviation of the PSF matching kernel, target PSF and initial rebinned PSF, respectively. We subsequently convolve the rebinned image with the PSF matching kernel κ .

4. Background and noise addition

For the background noise, we utilise the mosaic cutout without sources from actual observations and incorporate it into the images.

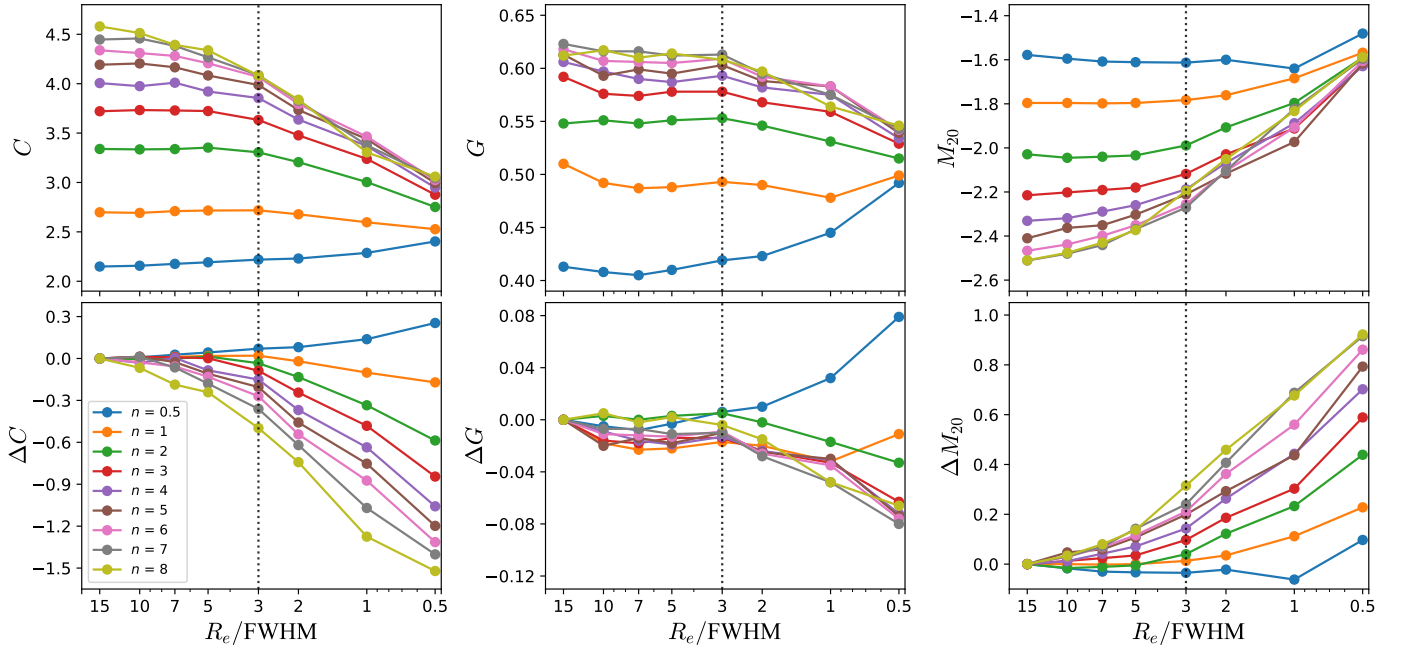


Fig. A.1. The measured concentration index (left), Gini coefficient (middle) and the M_{20} index (right) for the idealised mock images in CEERS survey as a function of the relative size of the galaxy (R_e/FWHM), with different colours representing different Sérsic indices. The top and bottom rows show the structural parameter (C , G , M_{20}) and the deviation from the intrinsic values (ΔC , ΔG , ΔM_{20}), respectively. This trend in each panel is similar to Fig. 15.